Site Map
Search
What's New
Help/Feedback
Contacts

Materials Research Society—The Materials Gateway

MRS ■ Electronic Library

Members Only | Preview Member Area | Join MRS
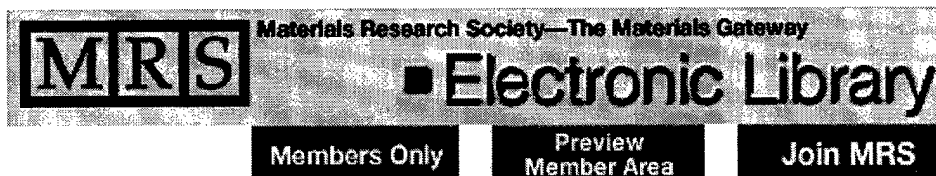
■ **Home**

■ **News**

■ **Society Information**

■ **Members Only**

■ **Membership**

■ **Join MRS!**

■ **Meetings**

■ **Materials Connections**

■ **Publications**

■ **Electronic Library**

■ **JMR**

■ **MRS Bulletin**

■ **Exhibits**

■ **Corporate Affiliates**

■ **Marketing Opportunities**

▓ **Webcasts**

■ **Bulletin Classifieds**

▓ **MRS Awards**

■ **Public Affairs**

■ **Materials MicroWorld**

2000 FALL MEETING PROCEEDINGS

Symposium M
Thermal Barrier Coatings--2000

Editors: Maria Arana Antelo, Nitin P. Padture, Bruce Pint, Sanjay Sampath, David J. Wortman

MRS Proceedings Volume 645E

Modeling Effects of Material Properties and Three-Dimensional Surface Roughness on Thermal Barrier Coatings M4.6
Michael L. Glynn, K.T. Ramesh, P.K. Wright, and K.J. Hemker

Phase Identification in Heated Thermal Barrier Coatings Using Microbeam X-ray Diffraction Combined with Quantitative X-ray Mapping M8.4
Jennifer R. Verkouteren, Ryna B. Marinenko, and David S. Bright

Quality Assurance Evaluation of Thermal Barrier Coatings by Electrochemical Impedance Spectroscopy M8.6
Jianqi Zhang, Danyash Tamboli, and Vimal Desai

Measuring the Properties of Diffusion Aluminide Bond Coat Layers With Microsample Tensile Testing M9.3
Deng Pan, P.K. Wright, and K.J. Hemker

A Numerical Model of Ratcheting in Thermal Barrier Systems M9.4
Anette M. Karlsson and Anthony G. Evans

Microstructural Characterization of Yttria-Doped Zirconia Coatings With Electron Microprobe Wavelength Dispersive Compositional Mapping M9.7
Ryna B. Marinenko, Jennifer R. Verkouteren, and David S. Bright,

Changes in Crystal Structure and Microhardness During Thermal Treatment of a NiCoCrAlY Alloy M9.13
Thomas Rehfeldt, Gerhard Schumacher, and Hellmuth Klingelhoeffer

In-Plane Cracking Behavior Near and Away From Interface of Thermal Barrier Coatings and Thermally Grown Oxides M9.15
Z. Zhang, J. Kameda, A. H. Swanson, and S. Sakurai

R&D Status and Needs for Improved EB-PVD Thermal Barrier Coating Performance M10.1
C. Leyens, U. Schulz, M. Bartsch, and M. Peters

DISTRIBUTION STATEMENT A
Approved for Public Release
Distribution Unlimited

20011001 018

MODELING EFFECTS OF MATERIAL PROPERTIES AND THREE-DIMENSIONAL SURFACE ROUGHNESS ON THERMAL BARRIER COATINGS

Michael L. Glynn, K.T. Ramesh, P.K. Wright[*] and K.J. Hemker
Johns Hopkins University, Mechanical Engineering, Baltimore, MD 21218
*GE-Aircraft Engines, Materials and Process Engineering Department, Cincinnati, OH 45215

ABSTRACT

Thermal barrier coatings (TBCs) are known to spall as a result of the residual stresses that develop during thermal cycling. TBC's are multi-layered coatings comprised of a metallic bond coat, thermally grown oxide and the ceramic top coat, all on top of a Ni-base superalloy substrate. The development of residual stresses is related to the generation of thermal, elastic and plastic strains in each of the layers. The focus of the current study is the development of a finite element analysis (FEA) that will model the development of residual stresses in these layers. Both interfacial roughness and material parameters (e.g.,modulus of elasticity, coefficient of thermal expansion and stress relaxation of the bond coat) play a significant role in the development of residual stresses. The FEA developed in this work incorporates both of these effects and will be used to study the consequence of interface roughness, as measured in SEM micrographs, and material properties, that are being measured in a parallel project, on the development of these stresses. In this paper, the effect of an idealized three-dimensional surface roughness is compared to residual stresses resulting from a grooved surface formed by revolving a sinusoidal wave about an axis of symmetry. It is shown that cylindrical and flat button models give similar results, while the 3-D model results in stresses that are significantly larger than the stresses predicted in 2-D.

INTRODUCTION

Thermal barrier coating (TBC) systems are comprised of four basic layers. The superalloy substrate, the bond coat, the oxide layer and the top coat all form the TBC system. Because of the interaction between these layers, the mechanical properties of one layer can effect the development of stresses in another layer. For this reason, a finite element model was developed to track the stresses that arise in each layer as a result of thermal cycling. Early TBC development equated durability of the TBC system to bond coat oxidation resistance [1]. However, the mechanical properties of the bond coat can also influence TBC life; a strong correlation between calculated out-of-plane tensile residual stresses in the top coat and TBC life has been presented [2]. In this light, it appears important to determine what contributes to the development of these residual stresses.

If all layers remain elastic, no residual stresses will arise. Consequently, at least one layer must behave inelastically in order for residual stresses to develop. Additionally, if all interfaces remain straight, no significant out-of-plane residual stresses will develop. Therefore, it is the combination of an interface roughness and plasticity that leads to significant out-of-plane residual stresses. Observations of the oxide layers in thermally cycled TBC's reveal clear evidence for interface roughening, see for example [3]. Additionally, stress relaxation of the bond coat layer has been measured for both plasma sprayed MCrAlY bond coats [4] and
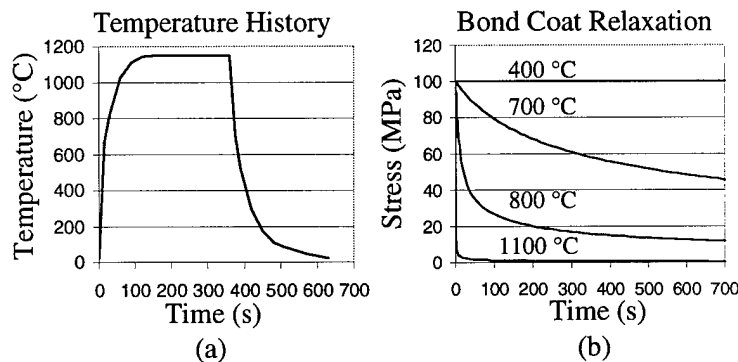
Figure 1. Input parameters for FEM calculations. (a) Temperature history for a typical burner rig thermal cycle. (b) Relaxation of the bond coat as a function of temperature.

diffusion aluminide bond coats [5]. The three FEM models presented in this paper were developed to explore the effects of geometry and interface roughness on the development of residual stresses in the TBC system. A long term goal of this project is the relation of these stresses to failure mechanisms and the prediction of TBC lifetimes.

MODELING

For each of the three models considered for this paper, the loading and properties were the same. Typical of a burner rig thermal cycle, the specimen was heated, held at temperature, then cooled (Fig. 1a) without any other applied loading. All of the layers in the TBC system were modeled with temperature dependent elastic properties taken from [5], and typical values are summarized in Table 1. The bond coat layer was allowed to relax at high temperatures (Fig. 1b) using the simple relationship, strain rate = A(stress)^n that was taken from [4]. Values for A and n are summarized in Table 2 as a function of temperature. The units of strain rate are s^{-1}, while the units of stress are Pa. All models were run using the ABAQUS finite element code.

In addition, the roughness of the oxide layer was characterized both before and after furnace cycling based on scanning electron microscope (SEM) images (Fig. 2). As can be seen in the figures, both the wavelength and the amplitude of the oxide roughness increase and the oxide

Table 1. Elastic Properties

	E (GPa)	ν	C.T.E. 10^{-6} (°C^{-1})
Substrate	205	0.27	15
Bond Coat	205	0.27	16
Oxide	375	0.30	8.5
Top Coat	30	0.30	10

Table 2. Bond Coat Stress Relaxation

| Temp (°C)	A	N
0	7.40E-70	3.2
200	1.04E-47	3.2
400	1.02E-38	3.2
600	7.59E-34	3.2
700	3.68E-32	3.2
800	8.64E-31	3.2
900	1.18E-29	3.2
1000	1.08E-28	3.2
1100	7.10E-28	3.2
1150	1.65E-27	3.2
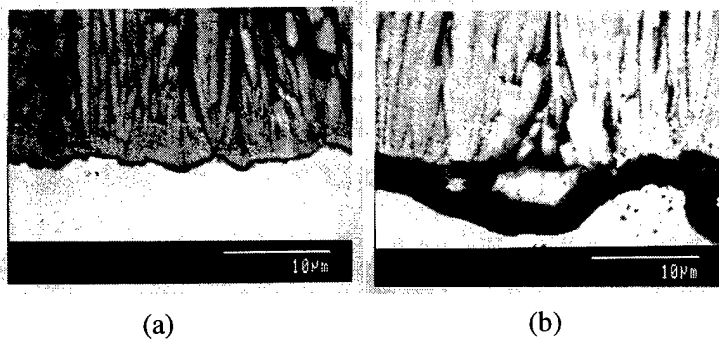
Figure 2. SEM images of the oxide layer (a) before and (b) after thermal cycling taken at the same magnification. Notice the thickening of the oxide layer as well as the increase of both the wavelength and amplitude.

layer thickens after thermal cycling. A crack can also be seen in the top coat layer after furnace cycling. Furthermore, the microstructure of the bond coat coarsens as a result of thermal cycling. Because of the depletion of aluminum from the bond coat layer to the oxide layer, in addition to the microscopic coarsening of the bond coat layer, it is likely that the mechanical properties of this layer change over the lifetime of the TBC system [5]. For simplicity, the mechanical properties of the bond coat layer were not varied as a function of TBC life, and the roughness was modeled as a sinusoidal wave with a wavelength of 25 µm and an amplitude of 5 µm.

Two different variables were considered in this study using a total of three different models. First, two separate geometries were analyzed because both cylindrical specimens and button specimens are used to assess TBC performance, see for example [5,7]. A cylindrical model with a two-dimensional interface roughness was compared to a button model with a two-dimensional interface roughness to examine the effects of geometry on stress development (Fig. 3). Second,
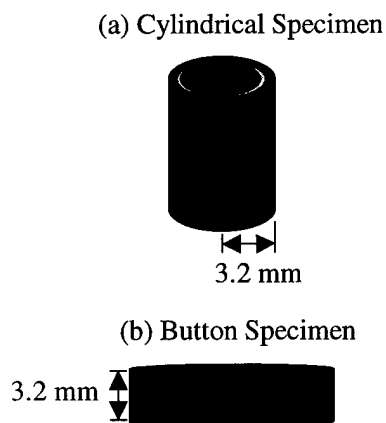
Figure 3. (a) A cylindrical and (b) a button specimen are considered in this study. Notice that the out-of-plane dimension is the same in each case.
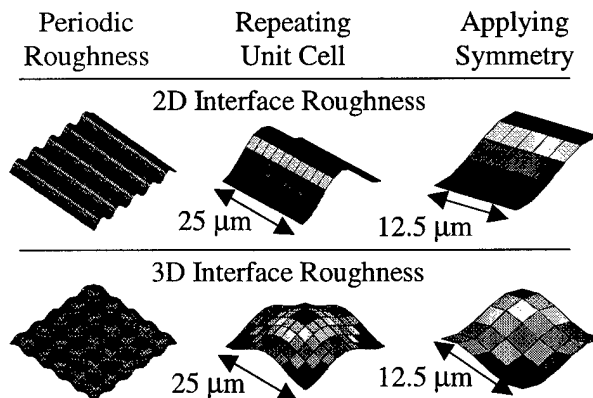
Figure 4. Two different interface roughnesses, a 2D and a 3D, are considered in this study. Shown in the figure is the periodic roughness over 5 periods, one repeating unit cell and finally the geometry analyzed after applying boundary conditions for each case.

M4.6.3

Figure 5. Out-of-plane dimensions for the TBC system. Note that only a small section of the substrate is pictured. Taken from P.K. Wright, Mat. Sci. Eng. A245, 1998
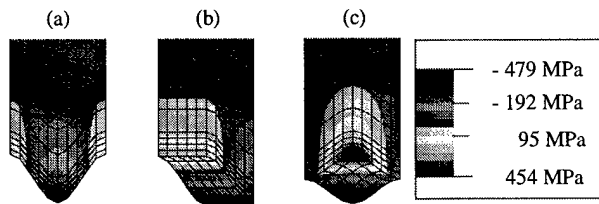
two different interface roughnesses were analyzed (Fig. 4). The same button model with a two-dimensional interface roughness was compared to a button model with a three-dimensional interface roughness to examine the effects of interface roughness on stress development. The out-of-plane dimensions for each model are the same, and they were determined from experimental observations. For each case, the 3.2 mm substrate was coated with a 65 μm bond coat, followed by a 3 μm oxide layer and finally capped with a 122 μm top coat; these dimensions were taken from the experimental observations shown in Fig. 5.

The cylindrical model is shown in Fig. 6(a). Due to the radial symmetry of the problem, axisymmetry was used to produce a two-dimensional model. Furthermore, a periodic boundary condition was used in the in-plane, or axial, direction. Therefore, a representative, periodic length of 25 μm, corresponding to the wavelength of the interface roughness, was used. The radial direction is the out-of-plane direction, and its dimensions were previously discussed. The resulting model is a solid cylinder with a grooved interface formed by revolving a sinusoidal wave about an axis of symmetry. As discussed earlier, the sinusoidal wave has a wavelength of 25 μm and an amplitude of 5μm.

The button model with a two-dimensional interface roughness is given in Fig. 6(b). As with the cylindrical model, periodic boundary conditions were used in the in-plane direction. But, unlike the cylindrical model, the in-plane dimensions for the button model are the x and y directions. The in-plane dimensions are further reduced using symmetry. Therefore, only 12.5 μm are modeled in each direction. For the case of the two-dimensional interface roughness, only the y direction has a sinusoidal wave. The out-of-plane dimensions are the same as those in the cylindrical model. The resulting model is a unit cell with a grooved interface. Again, the
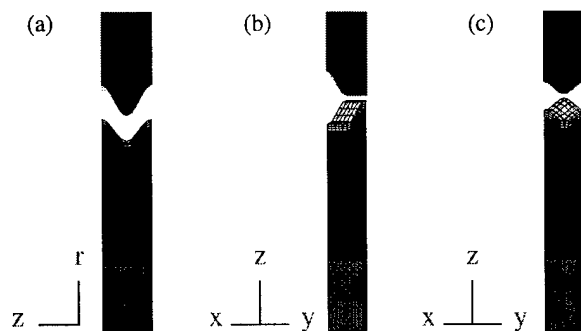
Figure 6. FEM models used to evaluate the effects of geometry and surface roughness on (a) a cylinder with 2D roughness, (b) a button with 2D roughness and (c) a button with 3D roughness. The top coat has been separated and rotated so the surface roughness can be seen. Note that the out-of-plane direction for the cylinder is the r direction, while for the button it is the z direction.

M4.6.4

(a)   (b)   (c)

- 479 MPa
- 192 MPa
95 MPa
454 MPa

Figure 7. *Out-of-plane residual stresses developed in the top coat after a thermal cycle in (a) a cylinder with 2D roughness, (b) a button with 2D roughness and (c) a button with 3D roughness.*

sinusoidal wave has a wavelength of 25 μm and an amplitude of 5 μm, although only half of the wavelength is modeled.

The last model discussed is the button model with a three-dimensional interface roughness (Fig. 6c). This model is very similar to the previously discussed model, except for the interface roughness. Both the x and y directions have a sinusoidal wave in this case. The resulting model is a unit cell with an idealized three-dimensional interface roughness. As before, the sinusoidal wave has a wavelength of 25 μm and an amplitude of 5 μm, although only half of the wavelength is modeled.

RESULTS AND DISCUSSION

Significant residual stresses were found to develop in the top coat after the thermal cycle described in figure 1. The maximum residual stresses in the top coat for the three different models are listed in Table 3, and the out-of-plane stress distribution is illustrated in Fig. 7.

Table 3. Top Coat Residual Stresses

Maximum Residual Stresses	Cylindrical Model 2D Interface	Button Model 2D Interface	Button Model 3D Interface
Out-Of-Plane Tensile (MPa)	250	249	454
Out-Of-Plane Compressive (MPa)	-392	-396	-479
In-Plane Tensile (MPa)	53	51	94
In-Plane Compressive (MPa)	-134	-125	-199

As previously reported, the residual stresses were found to arise as a result of the stress relaxation in the bond coat, while the out-of-plane residual stresses were related to the interface roughness. As illustrated in the above table, there is no significant change in residual stresses between the cylindrical model with a 2D interface roughness and the button model with a 2D interface roughness. However, the table shows an appreciable difference when comparing the 2D interface roughness to the 3D interface roughness for the button models. The tensile out-of-plane residual stress nearly doubles when comparing the 2D interface roughness to the 3D interface roughness. Because the out-of-plane tensile stress and in-plane compressive stress are related to failure in the TBC systems [2][8], it is important to consider the full three-dimensional interface roughness.

CONCLUSIONS

Significant residual stresses develop upon thermal cycling and are dependent on both bond coat properties and interface roughness. It is evident from experimental observations that thermal cycling also causes an increase in both the wavelength and amplitude of the interface roughness, thickening of the oxide layer, and coarsening of the microstructure in the bond coat. There is no significant difference in the residual stresses that are predicted using a cylindrical model with a 2D interface and a button model with a 2D interface. However, care must be taken when modeling the interface roughness. The out-of-plane residual stresses were found to be nearly double when a 3D interface roughness was modeled, as compared to a 2D interface roughness.

Because the mechanical properties of the bond coat layer and the roughness of the oxide layer play such an important role in the development of stresses, it is essential to characterize these layers. And, due to the dynamic nature of the TBC system, both of these layers need to be characterized as a function of TBC life. The FEA models developed in the present study are being coupled with microsample measurements of these material properties [5] and will be used to track the development of residual stresses in the various TBC layers.

ACKNOWLEDGEMENTS

REFERENCES

1. R.A. Miller, Oxidation-Based Model for Thermal Barrier Coating Life, *J. Am. Ceram. Soc.*, **67**, 517-521 (1984).
2. W.J. Brindley, Properties of Plasma Sprayed Bond Coats, Thermal Barrier Coatings Workshop Proceedings, *NASA Publication No. 3312* (1995).
3. V.K. Tolpygo and D.R. Clarke, Surface Rumpling of a (Ni,Pt)Al Bond Coat Induced by Cyclic Oxidation, *Acta Mater.*, **48**, 3283-3293 (2000).
4. W.J. Brindley and J.D. Whittenberger, Stress Relaxation of Low Pressure Plasma-Sprayed NiCrAlY Alloys, *Mat. Sci. Eng.*, **A163**, 33-41 (1993).
5. Deng Pan, P.K. Wright and K.J. Hemker, Measuring the Properties of Diffusion Aluminide Bond Coat Layers with Microsample Tensile Testing, *MRS Conference Proceedings*, this symposium, (2000).
6. B.L. Ferguson, G.J. Petrus and M. Ordillas, A Software Tool to Design Thermal Barrier Coatings, *NASA Phase I Final Report – Project No. 93-1-04.23-477* (1994).
7. P.K. Wright, Influence of Cyclic Strain on Life of a PVD TBC, *Mat. Sci. Eng.*, **A254**, 191-200, (1998).
8. Sung Ryul Choi, John W. Hutchinson, A.G. Evans, Delamination of Multilayer Thermal Barrier Coatings, *Mech. of Mater.*, **31**, 431-447 (1999).

Phase Identification in Heated Thermal Barrier Coatings using Microbeam X-ray Diffraction Combined with Quantitative X-ray Mapping

Jennifer R. Verkouteren, Ryna B. Marinenko, David S. Bright
Chemical Science and Technology Laboratory, National Institute of Standards and Technology, Gaithersburg, MD 20899, U.S.A.

ABSTRACT

Phase evolution in a yttria-partially-stabilized zirconia (Y-PSZ) thermal barrier coating (TBC) was studied by using quantitative electron probe x-ray mapping combined with microbeam x-ray diffraction. The as-sprayed coating contains a single t' phase with the composition of the feedstock material. After annealing at 1400 °C for 1 hour, the yttria content of the t' phase increases slightly to compensate for the formation of 0.06 mass fraction of a t phase containing 0.01 mole fraction $YO_{1.5}$. These results are in contrast to those determined by bulk x-ray and neutron diffraction, and therefore highlight the need for multiple techniques of phase analysis in Y-PSZ.

INTRODUCTION

Phase evolution during heating of Y-PSZ can have a significant effect on the stability of TBCs. Phase equilibria studies predict that, at elevated temperatures, yttria will diffuse from the desired metastable t' (tetragonal) phase to form a low-yttria t phase and a high-yttria c (cubic) phase [1, 2]. When the yttria content of the t phase reaches approximately 0.03 mole fraction $YO_{1.5}$ there is a martensitic transformation to an m (monoclinic) phase, with an increase in unit-cell volume. Experimental studies of the phase evolution in Y-PSZ TBCs have generally confirmed these predictions, both in plasma-sprayed coatings [3], and more recently, in coatings produced by electron-beam physical vapor deposition (EB-PVD) [4]. These studies used x-ray or neutron diffraction for phase analysis, with the yttria content of the phases determined on the basis of lattice parameters. The diffraction techniques are challenging due to overlap of the t and c phase diffraction patterns, with the result that most researchers are now utilizing the most advanced analytical procedures available, including Rietveld refinement [5] and whole-pattern fitting [6]. Although these procedures are superior to standard peak profiling techniques for the resolution of overlapping diffraction patterns, assumptions must be made that can affect both the qualitative and quantitative results. In particular, the presence of the c phase in a mixture of t and c phases can be missed [7], and selection of the incorrect phase assemblage can affect the measurement of lattice parameters.

In the present study, an independent test of the accuracy of diffraction techniques was accomplished by combining quantitative electron probe x-ray mapping with microbeam x-ray diffraction. The combination of the two techniques allows for the direct measurement of phase composition, and has the potential to directly tie a crystallographic phase to a specific composition. The results for phase percentages and compositions were compared to previously published neutron diffraction results [8] and to x-ray diffraction results.

EXPERIMENTAL DETAILS

Deposits of 5 mm thick plasma-sprayed TBC's were prepared using a nominal 0.08 mass fraction Y_2O_3 (0.087 mole fraction $YO_{1.5}$) feedstock powder as described in [8]. A portion of the as-sprayed material was annealed at 1400 °C for 1 hour. The two samples (as-sprayed and annealed) were cut in cross-section, polished, and carbon-coated. Wavelength-dispersive (WDS) electron microprobe quantitative x-ray maps were collected according to the procedures described in a separate publication in this volume [9]. A Rigaku[1] microdiffractometer with 3-axis rotation mounted on an 18 kW rotating anode was used for the microbeam x-ray diffraction experiments. A 10 μm wide Cu K beam was produced by means of a total internal reflection collimator. The position of the beam on the sample surface coincides with the geometric center of the diffractometer circle and is marked by reference to a microscope ocular cross-hair. The areas of interest from the compositional maps were analyzed in the microdiffractometer by first locating the contamination squares produced by the electron beam, and then by using physical features evident in the maps. Data were collected using a curved position-sensitive detector (PSD) calibrated to a standard Si powder (SRM 640b). The variability in intensity within each Debye ring was tested by using a phosphor imaging plate placed over the PSD.

Bulk x-ray diffraction was performed on the polished specimens using a Philips 1830 diffractometer with Cu K_α radiation generated at 40 kV and 55 mA. Appropriate divergence slits and masks were used to restrict the beam footprint to the sample surface for all measured angles. The data were collected from 5°-140° 2θ at a 0.02° 2θ step with a 2 s dwell time. Data were refined using the whole pattern fitting procedure in Powder Cell [10] and the crystallographic structural parameters of t and c $(Zr_{1-x}Y_x)O_{2-x/2}$ from [11]. Neutron diffraction with Rietveld refinement was performed independently by a separate group at NIST prior to this study [8].

DISCUSSION

The as-sprayed sample is compositionally homogeneous, with an average composition determined from the x-ray maps of approximately 0.087 mole fraction $YO_{1.5}$, equivalent to the feedstock composition. [Uncertainties in the compositional results are discussed in [9].] The annealed sample is not homogeneous, as shown in figure 1 by the presence of micrometer-sized areas of low yttria concentration (0.01 mole fraction $YO_{1.5}$) and high yttria concentration (0.15 mole fraction $YO_{1.5}$). The low yttria areas occupy a relative area of 6 ± 2 % in the compositional maps, based on a total sampled area of 0.0175 mm^2. The high yttria areas represent less than 1 % by area, and the remaining material has an average value of 0.09 mole fraction $YO_{1.5}$. The area percentages can be considered as

---

[1] Certain commercial equipment, instruments, or materials are identified to specify adequately the experimental procedure. Such identification does not imply recommendation or endorsement by the National Institute of Standards and Technology, nor does it imply that the materials or equipment identified are necessarily the best available for the purpose.

roughly equivalent to mass percentages due to the similarity in density of the phases and the lack of any obvious preferred orientation.

The bulk x-ray diffraction results for the as-sprayed sample are consistent with the compositional results, indicating the presence of a single t' phase with ≈ 0.09 mole fraction $YO_{1.5}$. The neutron diffraction results are in general agreement, although a c phase is also reported to be present at a concentration of 0.06 ± 0.03 mass fraction. Both x-ray and neutron diffraction find the m phase to be at or below 0.01 mass fraction.

0.15 mole　　　　0.09 mole　　　　0.01 mole
fraction $YO_{1.5}$　　fraction $YO_{1.5}$　　fraction $YO_{1.5}$
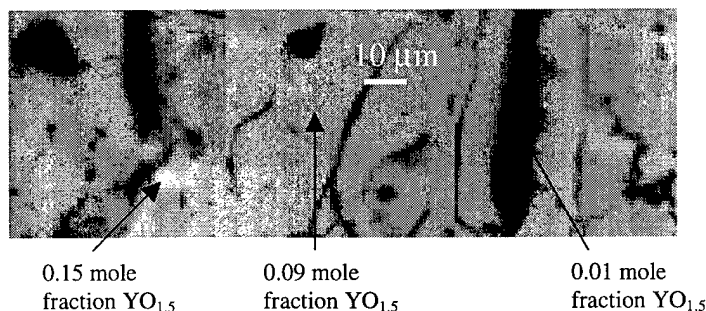
Figure 1. Three juxtaposed quantitative x-ray maps of annealed sample with gray level indicating yttria concentration from low (dark gray) to high (white). Cracks and voids are shown in black.

In contrast to the as-sprayed sample, the bulk x-ray and neutron diffraction results for the annealed sample do not agree with the compositional data. The data for the annealed sample from both diffraction techniques indicate that the original t' phase splits into a c phase with a higher yttria content (≈ 0.10 mole fraction $YO_{1.5}$) and a t phase with a lower yttria content (≈ 0.05 mole fraction $YO_{1.5}$). The results are shown in figure 2, where the
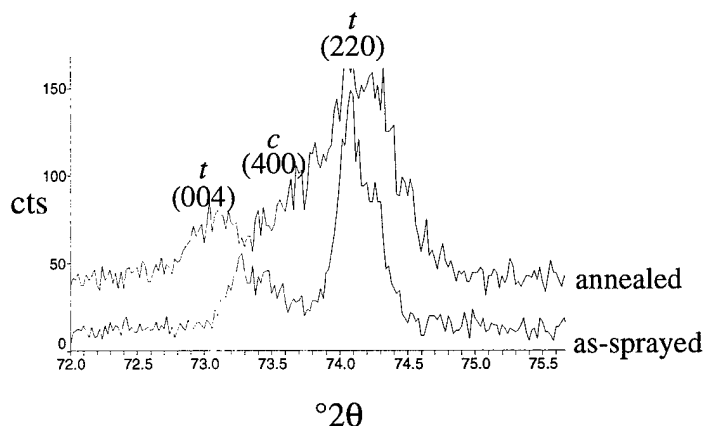
Figure 2. Bulk x-ray diffraction traces for annealed and as-sprayed Y-PSZ TBC. The patterns are consistent with an analysis of single phase t' for the as-sprayed sample, and 2-phase t and c for the annealed sample.

x-ray diffraction trace for the annealed sample has a saddle in the region attributed to the c (400) reflection, and an increased separation of the peaks attributed to the two t reflections, consistent with a lower yttria concentration. The proportions of the two new phases are $0.58 \pm .03$ mass fraction t, $0.41 \pm .03$ mass fraction c [8] for neutron diffraction and $0.69 \pm .08$ mass fraction t, $0.31 \pm .06$ mass fraction c for x-ray diffraction. [The m phase is at or below 0.01 mass fraction.]

The compositional data indicate that, after annealing, more than 90% of the original t' phase remains largely unchanged, except for a slight increase in yttria (from 0.087 to 0.09 mole fraction $YO_{1.5}$). The compositional data also indicate the presence of a relatively low concentration (0.06 mass fraction) of a second phase containing 0.01 mole fraction $YO_{1.5}$, which under equilibrium conditions should be an m phase, and a trace amount of a phase containing 0.15 mole fraction $YO_{1.5}$, which should be a c phase. The identity of the phase containing 0.01 mole fraction $YO_{1.5}$ was determined by using microbeam x-ray diffraction to probe the areas shown in figure 1. The critical microdiffraction data is given in figure 3, and the evidence strongly suggests that it is a t phase with lattice parameters consistent with a lower yttria content than the dominant t' phase. The phase is not monoclinic, as indicated by the absence of the two (111) m peaks near 30° 2θ. The sampling depth for compositional mapping is approximately 1 μm, compared with at least 16 μm for microdiffraction; therefore the microdiffraction results may not be exlusive to the low yttria phase.
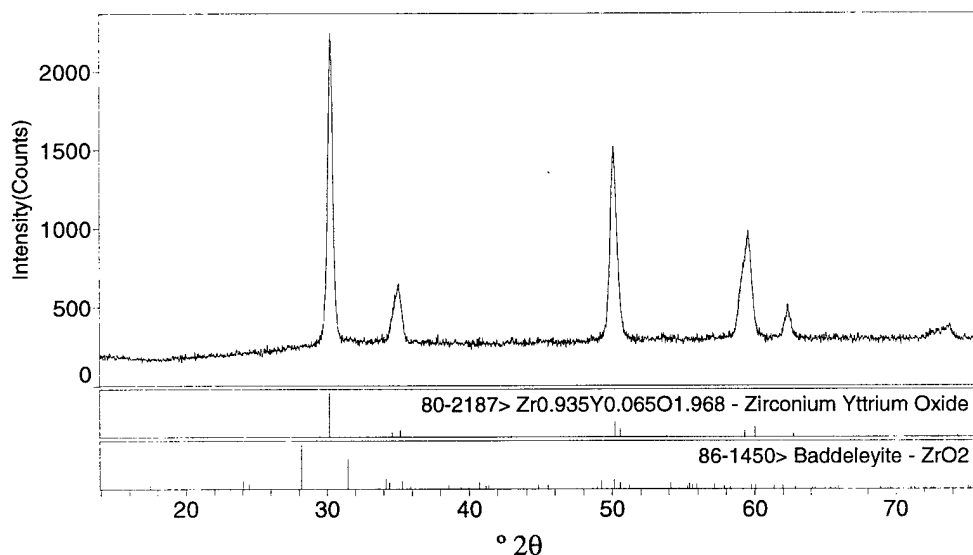
Figure 3. Microdiffraction results for 0.01 mole fraction $YO_{1.5}$ area in annealed sample showing the absence of any m phase peaks on either side of the 30°2θ t peak. Stick patterns for t (top) and m (bottom) phases from International Centre for Diffraction Data (ICDD) Powder Diffraction File (PDF) 2000.

Although we are sampling what appears to be a single compositional phase in the 0.09 mole fraction $YO_{1.5}$ areas, it is possible that each pixel is an average of multiple phases

with different compositions. The sampling volume at each pixel is approximated by a 1 μm diameter sphere, and could contain multiple phases if the crystallites are sufficiently small. This possibility was investigated by determining the crystallite size in the 0.09 mole fraction $YO_{1.5}$ areas. Electron backscatter diffraction (EBSD) patterns were collected from these areas using a Hitachi S-4500 field emission SEM equipped with a NORAN 32 bit Phase ID System. The EBSD patterns collected from these areas can be identified as either t, t', or c $(Zr_{1-x}Y_x)O_{2-x/2}$ (figure 4). Based on knowledge of the spatial resolution of EBSD [12], the crystallite size is determined to be between 100 and 500 nm. A calculation of the total number of spherical crystallites within this range of diameters at each pixel gives a number between 1000 and 10. With such a relatively small number of crystallites at each pixel, it is unlikely that the compositional data in the 0.09 mole fraction $YO_{1.5}$ areas represent an average of a t phase with 0.05 mole fraction $YO_{1.5}$ and a c phase with 0.10 mole fraction $YO_{1.5}$. In addition, the crystallite size in the 0.09 mole fraction $YO_{1.5}$ areas of the annealed sample appears comparable to the crystallite size in the as-sprayed sample, based on EBSD analysis, which would suggest that there was not considerable recrystallization in these areas. The 0.01 mole fraction $YO_{1.5}$ areas in the annealed sample do not yield EBSD patterns, which could be due to a crystallite size less than 100 nm, or to disturbance of the crystalline lattice due to defects, strain, etc. A smaller crystallite size or lattice disturbance could be explained by recrystallization of the material in the 0.01 mole fraction $YO_{1.5}$ areas.

Our interpretation of the compositional data combined with the x-ray microdiffraction data is that the t' phase from the as-sprayed sample is retained, with a slight increase in yttria content, in the annealed sample. A small proportion (0.06 ± 0.02 mass fraction) of a tetragonal phase with 0.01 mole fraction $YO_{1.5}$ and a trace amount of a phase with 0.15 mole fraction $YO_{1.5}$ are formed upon heating. Therefore, the results from compositional mapping/microdiffraction do not agree with the results from bulk x-ray and neutron diffraction for the annealed sample, even given the uncertainties associated with each technique.
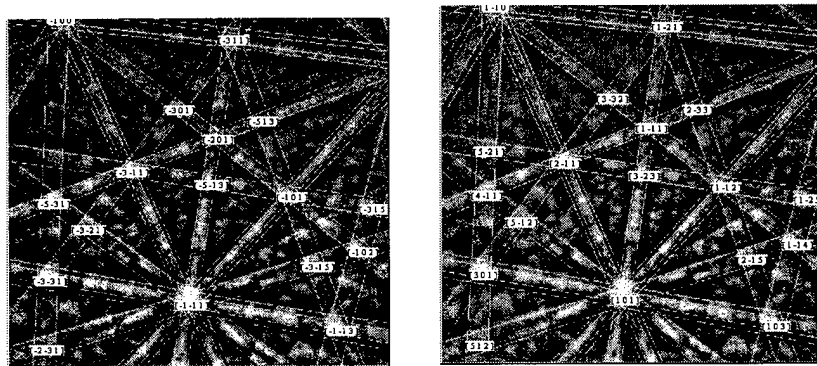
Figure 4. *EBSD pattern from 0.09 mole fraction $YO_{1.5}$ area in annealed sample. Simulated patterns in white were generated for t' $(Zr_{.94}Y_{.06})O_{1.97}$ (left) and c $(Zr_{.72}Y_{.28})O_{1.86}$ (right) and are equally well fit to the data.*

MM8.4.5

CONCLUSIONS

This study has shown that WDS quantitative mapping combined with x-ray microdiffraction is an alternative procedure for determining phase evolution in Y-PSZ TBCs. The diffusion of yttria can be directly measured, and new compositional phases can be located spatially with respect to textural features, such as cracks and voids. X-ray microdiffraction can then be used to determine the crystallographic phase associated with unique compositional areas. Although x-ray microdiffraction suffers the same drawbacks as bulk diffraction in analyzing overlapping t' and c phases, it offers the opportunity to restrict the analysis to a single compositional phase, thereby removing the requirement to resolve overlapping patterns.

The compositional changes determined by WDS mapping do not agree with results from bulk x-ray and neutron diffraction conducted using accepted procedures. This may be due to the inherent difficulties in separating overlapping diffraction patterns, or may point to insufficient constraints in relating lattice parameters to composition. X-ray microdiffraction analysis of low-yttria areas (0.01 mole fraction $YO_{1.5}$) demonstrate that a monoclinic phase is not present, as would be expected from phase equilibria studies. Therefore, results from WDS quantitative mapping/microdiffraction show that phase evolution in these materials may not follow the path predicted by phase equilibria studies.

REFERENCES

1. H.G. Scott, *J. Mater. Sci.*, **10**, 1527-35 (1975).
2. M. Yashima, M. Kakihana, and M. Yoshimura, *Solid State Ionics*, **86-88**, 1131-49 (1996).
3. R.A. Miller, J.L. Smialek, and R.G. Garlick, in *Advances in Ceramics, Vol. 3, Science and Technology of Zirconia I*, edited by A.H. Heuer and L.W. Hobbs (American Ceramic Society, Columbus, OH, 1981), pp. 241-253.
4. U. Schulz, J. Am. Ceram. Soc., **83**, 904-910 (2000).
5. L.C. Hammond and J.L. Cocking, *Powder Diffraction*, **11**, 75-79 (1996).
6. P. Scardi, E. Galvanetto, A. Tomasi, and L. Bertamini, *Surface and Coatings Technology*, **68/69**, 106-112 (1994).
7. D.N. Argyriou and C. J. Howard, *J. Appl. Crystallogr.*, **28**, 206-8 (1995).
8. J. Ilavsky and J. K. Stalick, *Surface and Coatings Technology*, **127**, 120-129 (2000).
9. R. B. Marinenko, J.R. Verkouteren, and D.S. Bright, this volume.
10. W. Kraus and G. Nolze, *J. Appl. Crystallogr.*, **29**, 301-3 (1996).
11. M. Yashima, S. Sasaki, M. Kakihana, Y. Yamaguchi, H. Arashi, and M. Yoshimura, *Acta Crystallogr., Sect. B: Struct. Sci.*, **B50**, 663-73 (1994).
12. F. J. Humphreys, *J. Micros.*, **195**, 170-185 (1999).

Quality Assurance Evaluation of Thermal Barrier Coatings by Electrochemical Impedance Spectroscopy

Jianqi Zhang, Danyash Tamboli and Vimal Desai
Advanced Materials Processing & Analysis Center, University of Central Florida,
Orlando, FL 32816-2450, U. S. A.

ABSTRACT

The technique of electrochemical impedance spectroscopy (EIS) was used to examine the behavior of intact thermal barrier coatings (TBC) at ambient temperature. Cross-sectional morphological examination of TBC was conducted by scanning electron microscope (SEM). By correlating the SEM visual examination with EIS data, TBC was characterized non-destructively. A model of EIS alternative current (AC) equivalent circuit was proposed to establish the relationship between the EIS elemental parameters in the circuit and the microstructural characteristics of TBC. A linear relationship was found to exist between the electrical impedance of TBC topcoat and the thickness of the topcoat. The porosity of TBC top coat showed a linear relationship with the capacitance of ceramic TBC, and the pore shape in the TBC topcoat was represented by the value of the electrical impedance of the pore. The result in the study has demonstrated that EIS can be used as a non-destructive evaluation (NDE) technique for quality assurance of TBC.

INTRADUCTION

Advanced turbine system engines are slated to operate at turbine inlet temperatures of nearly 2750°F so as to achieve 60% and higher overall efficiency. No currently used superalloys can withstand such high temperatures so that use of TBC is essential to reduce the substrate skin temperatures to acceptable level [1]. The successful application of TBC in land based gas turbines is a greater technical challenge compared to aero-engine applications because there are significant differences regarding the size/time/environment/stress duty cycles between these two systems. Land based gas turbine systems are expected to give inspection free long-term service while incurring harsh corrosive environment. Therefore, the long-term reliability of TBC is a far more critical concern in industrial gas turbines.

There are lots of disadvantages in currently used detection techniques that restrict their application. The techniques in characterizing the porosity or detecting the defects of TBC such as density, hardness and surface area measurements, optical microscopy, and mercury intrusion porosimetry are destructive. Conventional off-line NDE techniques such as radiography, eddy current and ultrasound to detect hidden flaws or debonding of TBC are much time-consuming. Small angle neutron scattering (SANS) [2] and nuclear magnetic resonance (NMR) imaging [3] techniques recently arouse great interest in detecting pores and cracks of TBC. However, the interpretation of SANS and NMR data is highly speculative. Reports show that thermal wave imaging is a rapid non-contact inspection technique capable of locating defects near the surface of 1~2 mm thick

samples by monitoring surface temperatures. Acoustic microscopy imaging can detect defects in structural materials by comparing the relative stiffness of the measured samples [4]. In addition, piezospectroscopy [5] has also been reported non-contact NDE techniques by measuring the internal stresses of thermally grown oxide (TGO) underneath the TBC topcoat. However, these techniques provide limited information regarding the failure of TBC. Impressively, there is a severe lack of methodology that can be steadily used for the detection of industrial TBC. As a result, development of NDE techniques capable of determining the coating quality economically and easily becomes paramountly important.

EIS is a widely used NDE technique in evaluating and monitoring the properties of organic coatings in aqueous solutions [6]. It is ideally suited for monitoring multi-layer systems. TBC is a typical multi-layer system. As a result, EIS was applied in this study to characterize the microstructure and morphological properties of TBC.

EXPERIMENTAL DETAILS

Air plasma sprayed 8%wt Y_2O_3 partially stabilized ZrO_2 TBC samples were obtained from the Siemens-Westinghouse Power Corporation. The specimens were cut into two pieces: one piece was used to examine the cross-sectional morphology of the coating using SEM while the other half was evaluated by EIS.

The morphological examination of the TBC samples was conducted using JEOL 4500 scanning electron microscope. The SEM morphological observation of TBC can provide such information as TBC topcoat thickness, porosity and pore structure. The EIS measurement was performed at room temperature in an EG&G PARC Model K0235 flat cell with a volume of 300 milliliters. Figure 1 shows a typical set-up for the EIS measurement. The TBC sample was used as
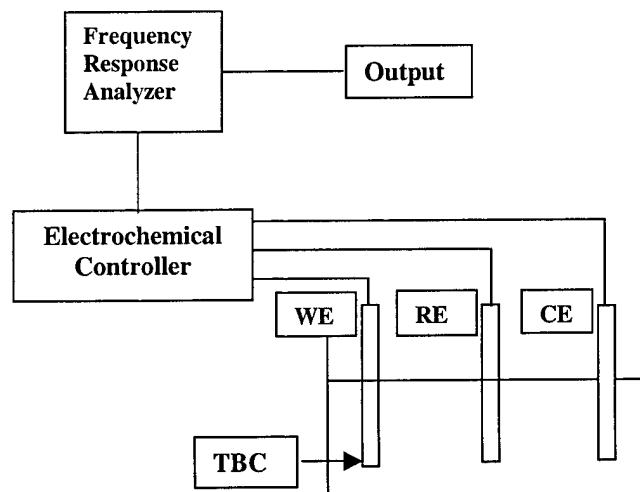
Figure 1. A typical setup of EIS measurement system

working electrode. A platinum mesh was used as counter electrode and an Ag/AgCl electrode as reference. 0.01M $[Fe(CN)_6]^{-3}/[Fe(CN)_6]^{-4}$ electrolyte was used in the EIS test because of its highly reversible redox characteristics. The electrode system was connected to a Zahner-IM6e EIS measurement system. A sinusoidal voltage perturbation of 20 mV amplitude was input to the system with a frequency range of 10^{-3}-10^{+6} Hz at the open circuit potential, and the system response was recorded as a Bode plot or/and a Nyquist plot.

DISCUSSION

A typical EIS Bode plot of the TBC samples is shown in Figure 2. A model of EIS equivalent ac circuit for intact TBC was suggested as shown in Figure 3.
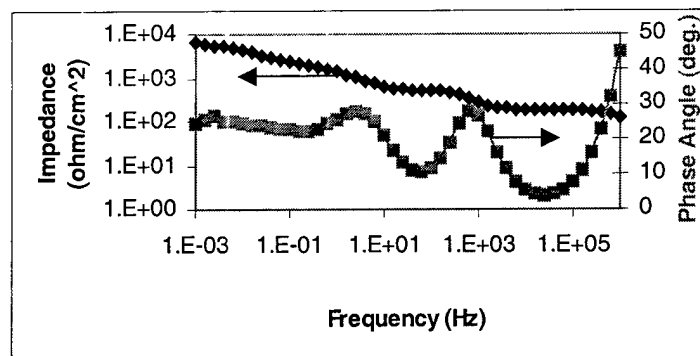

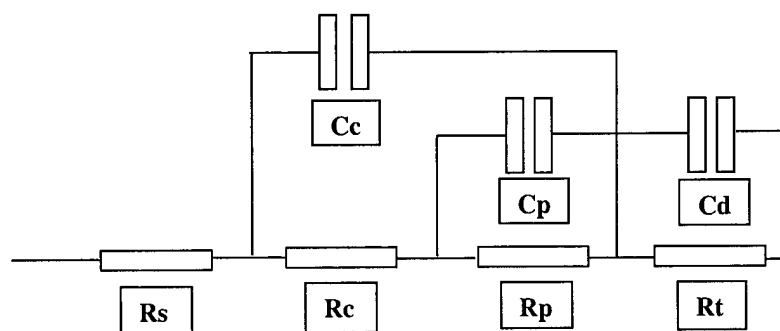Figure 2. A typical EIS Bode plot of intact TBC samples

Figure 3. An EIS equivalent a.c. circuit model for intact TBC

According to the model as shown in Figure 3, the impedance (Z) of the circuit can be expressed as:

$$Z(\omega) = R_s + \{ \, [\, R_c + (\, j\omega C_p + R_p^{-1})^{-1} \,] \, ^{-1} + j\omega C_c \, \}^{-1} + (\, j\omega C_d + R_t^{-1})^{-1} \qquad (1)$$

Where Z is the impedance of the system; R_s the solution resistance between the reference electrode and the TBC topcoat surface; R_c the resistance of the ceramic top coat and C_c ceramic topcoat capacitance, and the corresponding relaxation frequency of these two components is represented by 1 MHz phase peak as shown in Figure 2; R_p the summation resistance of the defects (such as pores, cracks) in the ceramic topcoat and C_p the summation capacitance of the defects in the ceramic topcoat, and their relaxation frequency is signified by the phase peak of about 1000 Hz as shown in Figure 2; R_t transmission resistance of the double layer at the interface between the ceramic topcoat and metallic bond coat and C_d the capacitance of the double layer at the interface between the ceramic topcoat and metallic bond coat, whose relaxation frequency corresponds to the phase peak at about 1 Hz as shown in Figure 2; ω angular frequency of the input sinusoidal wave and j sign of the imaginary part of complex.

Following relationships can be easily found from the EIS and SEM examination of as received APS-processed TBC samples. The TBC topcoat thickness is proportional to the ceramic impedance as shown in Figure 4. The topcoat porosity has a linear relationship with ceramic capacitance, as shown in Figure 5. The pore shape (type of defects) in the topcoat can be represented by the value of pore impedance as follows: Large oval pores in TBC topcoat (pore diameter over 12μm) corresponds to EIS values of Rp<350 ohms. Medium oval pores (pore diameter between 8-12μm) corresponds to 350<Rp<450 ohms. Small oval pores (pore diameter smaller than 8μm) in topcoat gives a value of Rp about 500 ohms. Interestingly, transverse cracks were identified by values of Rp>550 ohms.
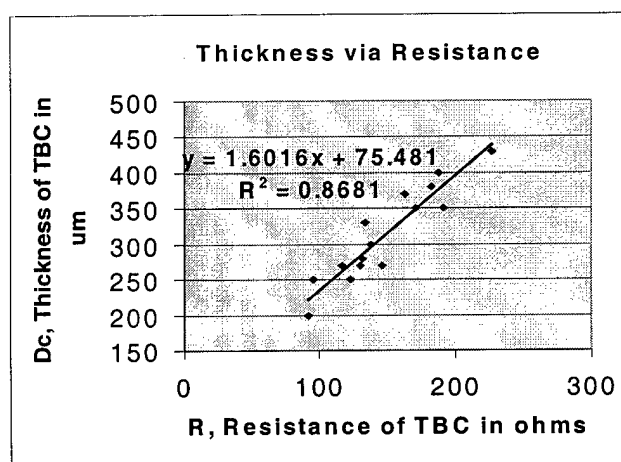

Figure 4. TBC topcoat thickness (Dc) is proportional to ceramic resistance (Rc)

M8.6.4
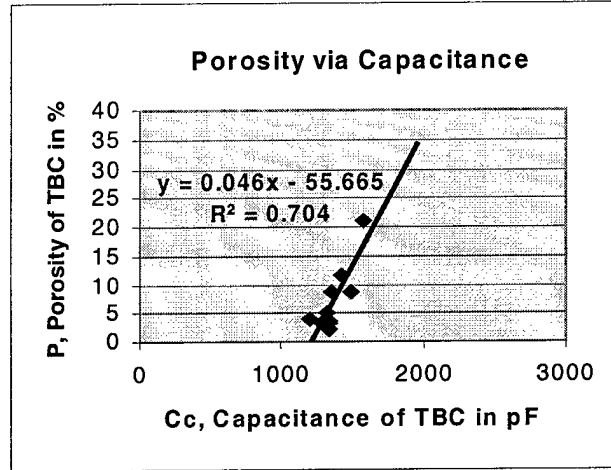
Figure 5. *A linear relationship exists between the ceramic porosity (P) and the pore capacitance (Cc)*

The linear relationship between topcoat thickness and ceramic impedance is easily understandable. TBC topcoat impedance depends on the values of TBC resistivity ρ, thickness Dc and tested area A according to Ohm's law, i.e.:

$$Rc= \rho \ (Dc/A) \tag{2}$$

If TBC samples possess a similar porosity they have a similar value of resistivity. Therefore the impedance of TBC is directly proportional to its thickness. On the other hand, since TBC can be taken as a composite which consists of ceramic and porosity, the capacitance of TBC (Cc) would be the sum of the ceramic capacitance (Cc') and porosity capacitance (Cp) (two capacitors are in parallel), i.e.:

$$
\begin{aligned}
Cc &= Cc'+Cp \\
&= \varepsilon_0\varepsilon_1(A/Dc)(1 - P) + \varepsilon_0\varepsilon_2(A/Dc)(P) \\
&= \varepsilon_0\varepsilon_1(A/Dc) + \varepsilon_0(\varepsilon_2 - \varepsilon_1)(A/Dc) \ P \\
&= k_1 + k_2 \ P
\end{aligned}
\tag{3}
$$

Where ε_0, ε_1 and ε_2 are dielectric constants corresponding to the vacuum, ceramic TBC and electrolyte dewelling in the pores; Dc the ceramic topcoat thickness. Therefore, k_1 and k_2 are constants determined by TBC ceramic and electrolyte used for EIS. As a result, TBC capacitance (Cc) is proportional to its porosity (P). Finally, the impedance of pores (Rp), according to Ohm's law, can be expressed as:

$$Rp= \rho_p \ (Dp/Ap) \tag{4}$$

Suppose we can take the pores as of cubic shape where Dp is the length of the pores and Ap the cross-sectional area of the pores, equation (4) can be transformed into:

$$Rp \sim \rho_p / Dp \qquad (5)$$

Therefore, small size pores correspond to large pore impedance. For the cracks transverse the topcoat, their corresponding impedance is much higher as the pore distance Dp is greater.

The parameters of TBC such as topcoat thickness, porosity and type of defect are very important in evaluating TBC quality. Consequently, the results establish EIS as an ideal evaluation technique for TBC quality assurance.

CONCLUSIONS

This study shows that EIS has a great promise to be a NDE technique for the quality assurance evaluation of TBC. A model of an EIS AC equivalent circuit was proposed to establish the relationship between EIS signals and TBC morphological parameters. From the model, the TBC topcoat thickness can be estimated by the value of ceramic impedance as measured by EIS. The porosity of the TBC topcoat can be determined by the ceramic capacitance value and the pore size/defect in the ceramic can be evaluated by the value of pore impedance.

REFERENCES

1. G. L. Erickson, Superalloy Developments for aero and industrial gas turbines, *Proceedings of ASM 1993 Materials Congress Materials Week' 93*, October 17-21, 1993, Pittsburgh, Pennsylvania.
2. U. Betz, A. Sturm, J. F. Loffler and W. Wagner, A. Wiedenmann, H. Hahn, Microstructural development during final-stage sintering of nanostructured zirconia based ceramics, *Materials Science and Engineering* **A281** (2000), 68-74.
3. A. Klemm, H-P. Muller and R. Kimmich, Evaluation of fractal parameters of percolation model objects and natural porous media by means of NMR microscopy, *Physica* **A266** (1999), pp.242-246.
4. J. D. Achenbach, Quantitative nondestructive evaluation, *International Journal of Solids and Structures* **37** (2000), pp.13-27.
5. R. J. Christensen, D. M. Lipkin and D. R. Clarke, Nondestructive evaluation of the oxidation stresses through thermal barrier coatings using Cr^{3+} ciezospectroscopy, *Applied Physics Letter*, **69** (24), 9 December 1996, pp.3754-3756.
6. K. Homma, H. Kihira and S. Ito, Application of alternating current impedance method to the evaluation of coating deterioration, *Corrosion-91*, 1991, Paper # 483.

MEASURING THE PROPERTIES OF DIFFUSION ALUMINIDE BOND COAT LAYERS WITH MICROSAMPLE TENSILE TESTING

DENG PAN, P.K. WRIGHT* and K.J. HEMKER

Department of Mechanical Engineering, The Johns Hopkins University, Baltimore, MD 21218
* GE-Aircraft Engines, Materials and Process Engineering Department, Cincinnati, OH 45215

ABSTRACT

The bond coat layer plays an important role in the TBC system by providing oxidation resistance and a foundation for the ceramic top coat. The thermal cyclic durability of a TBC is thought to be strongly dependent on the physical and mechanical properties of the bond coat layer. Attempts to measure these properties for as-deposited and thermally cycled diffusion aluminide bond coats have been greatly inhibited by the limited thickness (~60 μm) of these coatings. In the present study, novel high temperature microsample tensile testing technique is employed to measure the Young's modulus (E), coefficient of thermal expansion (CTE), yield strength and stress relaxation behavior of an as-deposited (Ni, Pt)Al bond coat in the temperature range of 25 °C to 1150 °C. Preliminary results for these material parameters are reported here. They are being used as material inputs for an independent finite element analysis (FEA) study of the development of stresses in the TBC layers during thermal cycling.

1. INTRODUCTION

Thermal barrier coatings (TBC) are commonly used in commercial gas turbine engines to provide a thermal insulation between the hot gas stream and engine components. The interest in TBCs has grown continuously over the last 20 years, thanks in large part to their positive effect on the performance and durability of the turbine engines [1-3]. A detailed understanding of the micro-mechanisms that cause TBC spallation and failure has not, to date, been well elucidated.

One of the key components in a TBC system is the bond coat, which provides the oxidation resistance and acts as a foundation for the ceramic top coat. The mechanical properties of the bond coat have been shown to play an important role in the study of failure mechanism and life prediction of the TBC system [4]. To date, no investigations of the properties of diffusion aluminide bond coats, which have thickness of less than 60 μm, have been reported. Characterization of the mechanical behavior of the bond coat layer is, however, needed to provide a more comprehensive understanding of the development of stresses in the TBC system during thermal cycling. The present study is motivated by a desire to measure the Young's modulus (E), coefficient of thermal expansion (CTE), yield stress (σ_y) and stress relaxation behavior of a single phase diffusion aluminide bond coat layer as a function of temperature.

The development of a "microsample" tensile testing at JHU has greatly facilitated the mechanical testing of materials that are only available in small quantities or limited dimensions, as free-standing microsample specimens with a thickness of 25-500 μm and gage widths of 100-800 μm are routinely tested by this technique. Detailed descriptions of microsample testing are

given in [5-7]. To date, microsample testing has been used to measure the mechanical properties of a wide range of materials, including but not limited to: polysilicon thin films [8,9]; LIGA Ni, Cu and Permalloy [10,11]; single crystalline TiAl [12]; fully–lamellar and polysynthetically twinned TiAl based alloys [13]; nanocrystalline Ni, Cu and Al [14,15].

2. EXPERIMENTAL PROCEDURES

Samples of a single crystal superalloy, Rene N5 [16], were coated with a PtAl diffusion aluminide bond coat, and following that, an electron beam physical vapor deposition process was used to deposit a Yttria-stabilized Zirconia thermal barrier coating [17]. Prior to fabricating the bond coat specimens the ceramic coating was removed using a chemical process which left the bond coat intact.

Microsample bond coat specimens were prepared in the following way. The bond coat layer of the as-bond-coated button was scalped from the underlying substrate using a wire electro-discharge machine (EDM). This slice was ground to a uniform thickness of 150 μm with a lapping machine. Dog-bone shaped microsamples were then punched out of the slice employing a sinking EDM with a mirror-finish controller and a specially shaped graphite electrode. Each microsample has an overall dimension of 4mm by 1.7mm and is 500 μm wide in the gage section, see Fig. 1. The as-punched microsamples were mechanically ground and polished with a tripod polisher. This final polishing step produced a mirror finish on both faces and thicknesses of 20 to 50 μm with all unwanted layers (thermal grown oxide and substrate) removed. Great care was taken to assure the flatness and parallelism of both surfaces of the microsample. Platinum lines were then deposited on the gage section using a focused ion beam (FIB). Those lines were 250 μm apart, had dimensions of 45 μm long by 2 μm wide by 0.55 μm high, and served as the reflective markers for the non-contact Interferometric Strain/Displacement Gage (ISDG) technique for measuring strain. The microsample tensile machine and ISDG used in this study follow the designs of Sharpe [5] and Zupan [18]. In the high temperature tests, the specimen was heated resistively by passing a current through it, and a calibrated InGaAs optical pyrometer was employed to measure the temperature.

3. RESULTS AND DISCUSSION

The cross-sectional optical micrograph in Fig. 2 shows that the as-received bond coat layer was approximately 60 μm thick and comprised of two layers: a relatively homogeneous layer (~30 μm) and a diffusion layer (~30 μm) which contained a significant volume fraction of precipitates. Elemental analysis of the precipitates in the diffusion layer evidenced a high content of heavy elements (e.g. W, Ta) that can be traced back to the superalloy substrate. The microsamples
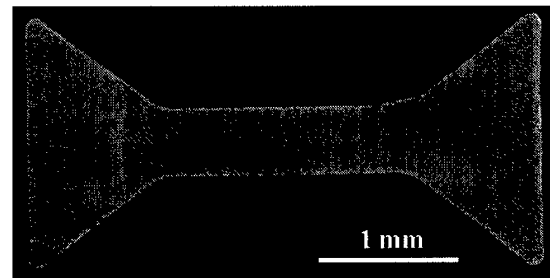
Fig.1. An example of a microsample that illustrates the shape and size of specimens used in this study.

tested for this study contain a portion of both layers.

Stress and strain curves of the bond coat specimens were measured under a variety of temperatures and typical curves are shown in Fig. 3. As depicted in Fig. 3(a), no obvious plastic deformation was observed at temperatures of 25 °C up to 500 °C. Below 600 °C the microsamples failed in a brittle manner with a wide variation in fracture strengths. Above 650 °C, clear plastic yielding was observed. Two examples of high temperature plasticity are given in Fig. 3(b).

The measured values of the yield strength are given as a function of temperature in Fig. 4. The yield strength decreased dramatically with increasing temperature. The relatively low strengths measured at 1150 °C (approximately 25 MPa) are comparable with reported values for NiAl [19].
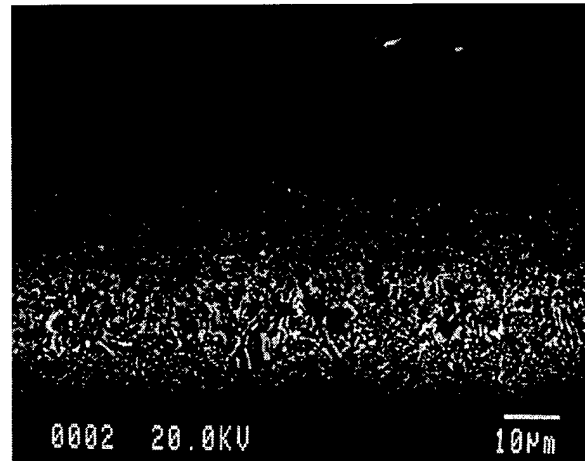
Fig.2. The cross section of bond coat layer. The bright spots in the diffusion layer are precipitates of heavy elements. Great care was taken during polishing to assure flat and parallel surfaces.

(a)

(b)
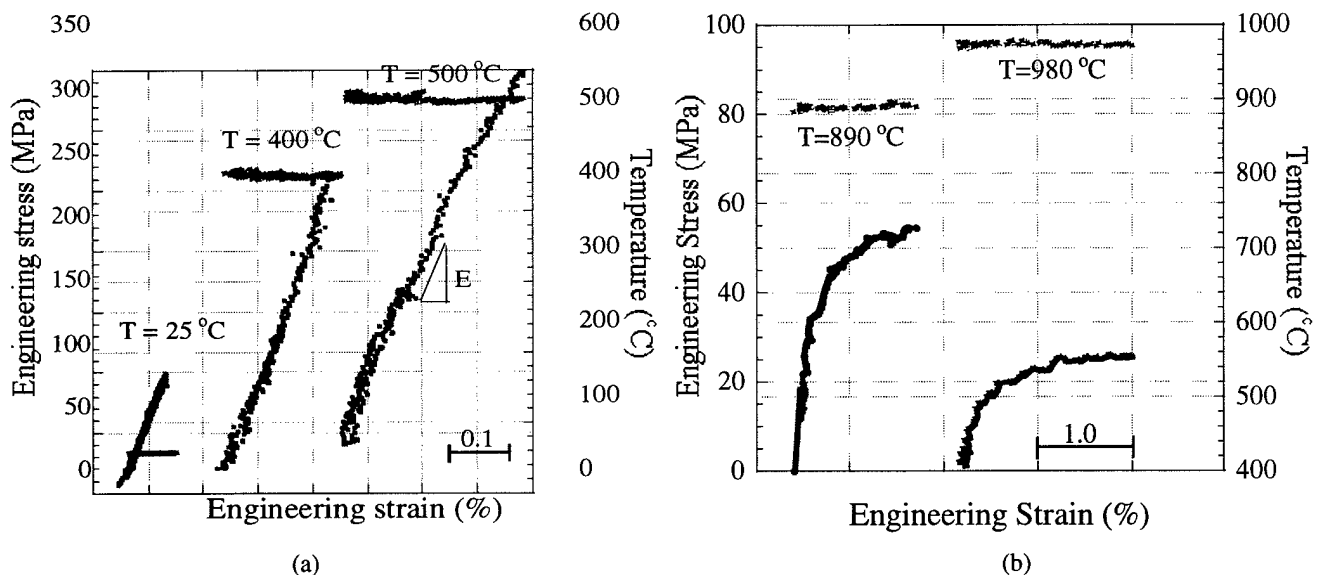
Fig. 3 (a) Load-unload curves at 25 °C, 400 °C and 500 °C. Loading remained in the plastic region, and the highest stress in each curve does not represent the actual fracture strength at that temperature. (b) The stress-strain curves at 890 °C and 980 °C. Extensive plasticity was observed at these temperatures. Horizontal traces show temperature for each test.
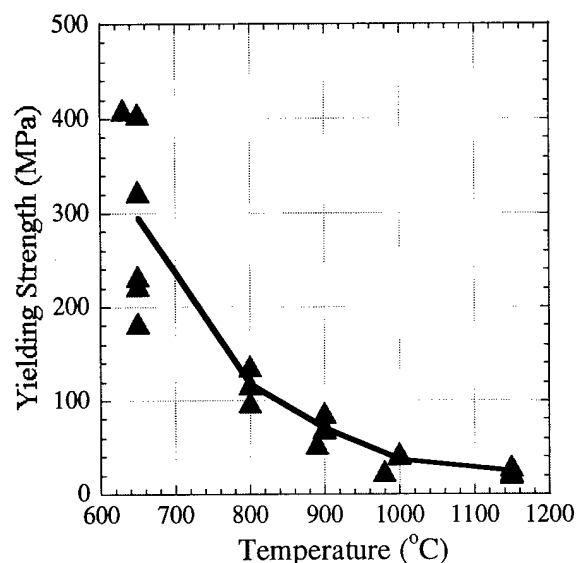
Fig. 4. Yield strength as a function of temperature. The strength drops dramatically with increasing temperature.
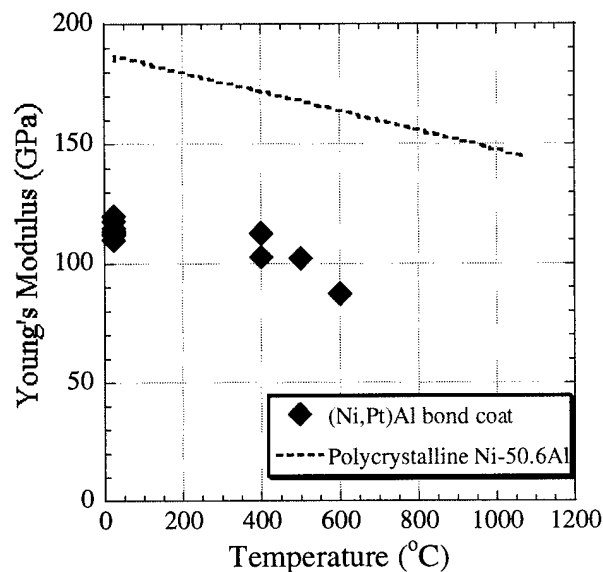
Fig. 5. Young's modulus vs. temperature. The E at room temperature is about 118 GPa, which falls in the range of 117 and 125 GPa of (001) texture NiAl.

The Young's modulus was measured as a function of temperature and is presented in Fig. 5. The modulus of the bond coat has been found to fall off gradually with temperature. It should be noted that the modulus at temperatures higher than 600 °C was not determined due to the influence of creep at these temperatures. Absolute values of the measured bond coat moduli are significantly lower than have been reported for polycrystalline NiAl [20]. However, the Young's modulus of NiAl has been shown to be strongly dependent on crystallographic orientation and the following calculation has been undertaken to determine the role that texture may have on the measured bond coat properties. The stiffness matrix (C_{11} = 199GPa, C_{12} = 137GPa, C_{44} = 116GPa) reported by Rusovic *et al* [21] has been used to calculate Young's modulus for all directions in the (001), (011) and (111) close-packed planes. Voigt [22] and Reuss [23] averages of the values in these planes are given in Table 1. The values reported in Table 1 would be expected to correspond to the in-plane moduli of a film that has an out-of-plane texture of [001], [011] or [111]. The experimental data was found to be in good agreement with the calculated modulus for a [001] textured coating. Experiments to measure the texture of the bond coat are underway.

Table 1. The Average E in Certain Texture of NiAl			
E(GPa)	(001) plane	(011) plane	(111) plane
Voigt	125	184	181
Reuss	117	159	181
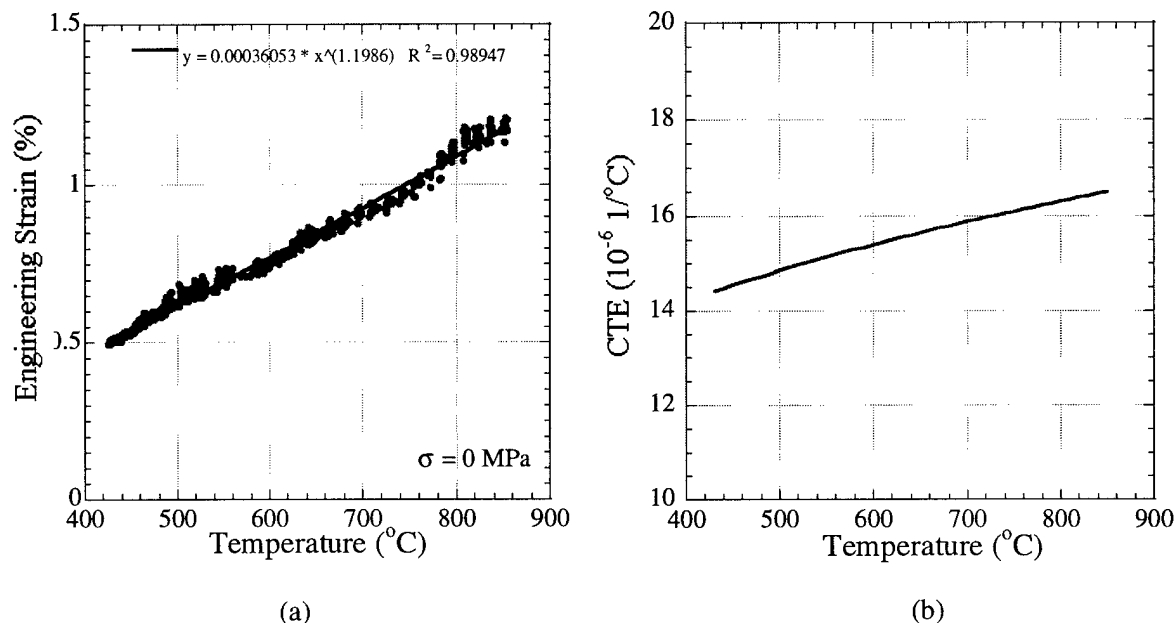
Fig. 6 (a) The measured strain-temperature curve and representative curve fit. (b) The CTE data obtained from the curve fit at the temperature range of 400 °C to 850 °C. Above 850 °C creep stain hindered the CTE measurement.

A strain versus temperature curve was obtained for a microsample that was heated from room temperature to 1000 °C under zero applied stress. The CTE of this microsample was determined by a fitting polynomial to the experimental data and then taking the partial derivative of that polynomial with respect to temperature. The results are shown in Fig. 6. The CTE of the bond coat was measured to be between 14 and 17 $\times 10^{-6}$ 1/°C in a temperature range of 400 to 800 °C, which is comparable with the CTE values reported by Wright et al [24].

The stress relaxation behavior of the single-phase (Ni, Pt)Al bond coat was investigated under four different temperatures: 400 °C, 650 °C, 900 °C, and 1150 °C. The results are shown in Fig. 7. No appreciable relaxation was observed at temperatures of 400 °C or below. By comparison, significant
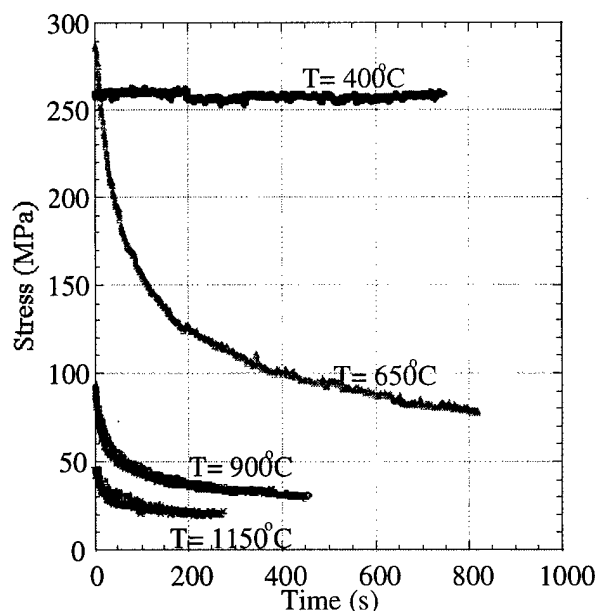
Fig. 7. The stress relaxation resistance of this (Ni, Pt)Al bond coat.

relaxation was recorded at higher temperatures. At 1150 °C an applied stress of 45 MPa was reduced to 20 MPa in less than 5 minutes. A comparison of the data shown in Fig. 7 with the published data for a MCrAlY bond coat by Brindley et al [4] suggest that the (Ni, Pt)Al bond coats are significantly more creep resisted than the previously predicted MCrAlY bond coats.

4. CONCLUDING REMARKS

The mechanical properties (E, CTE, σ_y, $\Delta\sigma_{relax}$) of a commercial bond coat were investigated in a temperature range from the ambient to 1150 °C using a novel high temperature microsample tensile testing technique. The material parameters obtained in the present study were compared with literature values for NiAl. The results suggest that the sample preparation and high temperature microsample testing techniques developed herein can be used to characterize the mechanical properties of thin film bond coat alloys.

5. ACKNOWLEDGEMENT

6. REFERENCES

1. F.O. Soechting, *TBC Workshop Proceedings*, 1, (1995)
2. R.A. Miller, TBC *Workshop Proceedings*, 17, (1995)
3. A. Maricocchi *et al*, *TBC Workshop Proceedings*, 79, (1995)
4. W.J. Brindley, *TBC Workshop Proceedings*, 189-202, (1995)
5. Sharpe, W. N., Jr. *et al*, *J. of Microelectromechanical Systems*, 6, 193-199 (1997).
6. Sharpe, W. N., Jr. and Yuan B., MRS Proceedings, 505, 51-56, (1998).
7. M. Zupan and K.J. Hemker, *Metal. Mater. Trans.*, 29A, 65-71, (1998).
8. W.N. Sharpe, Jr. *et al*, *SPIE*, 2880,78, (1996)
9. W.N. Sharpe, Jr. *et al*, *Proc. 10th IEEE Int. Workshop on MEMS*, 424, (1997)
10. W.N. Sharpe, Jr. *et al*, *SPIE*, 3512, 130, (1999)
11. W.N. Sharpe, Jr. *et al*, *MEMS*, ASME DSC-62/HTD-354, 93, (1997)
12. M. Zupan *et al*, *MRS Symp. Proc.*, 460, 171, (1997)
13. C.J. Boehlert *et al*, *International Symp. on Gamma Titanium Aluminides*, TMS, 669, (1999)
14. M. Legros *et al*, *MRS Symp. Proc.*, 457, 273, (1997)
15. M. Legros *et al*, *Phil Mag A*, 80,1017, (2000)
16. W.S. Walston *et al*, *Superalloys 1996*, Ed., R.D. Kissinger, *et al*, TMS, 27-34, 1996
17. D.J. Wortman *et al*, *Materials Science and Engineering*, A121, 433-440 (1989)
18. M. Zupan *et al*, *Experimental Mechanics*, in press
19. R.T. Pascoe *et al*, *Phys. Stat. Solidi.*, 29, 357, (1968)
20. C.A. Moose, Master thesis, Pennsylvania State University, (1991)
21. N. Rusovic *et al*, *Phys. Stat. Solidi.*, (A) 44, 609, (1977)
22. W. Voigt, *Lehrbuch der Krystallphysik*, (1910)
23. A. Reuss, *Zeitschrift fur Angewandte Mathematik und Mechanik*, 9, 49 (1929)
24. P. K. Wright *et al*, *Current Opinion in Solid State and Materials Science*, 4, 255 (1999)

A numerical model of ratcheting in thermal barrier systems

Anette M. Karlsson and Anthony G. Evans
Princeton Materials Institute, Princeton University, Princeton, NJ 08540

ABSTRACT

Morphological instabilities in thermally grown oxide, observed in a range of thermal barrier systems, have been simulated by developing and using a numerical code. The simulations are based on a range of phenomena and constituent properties, such as plasticity in the bond coat and growth strains in the TGO at high temperature. One of the key implications is that the incidence of reverse yielding upon reheating is a necessary condition for morphological instabilities. That is, whenever the condition for reverse yielding is satisfied during the initial cycles, the imperfection amplitude increases with thermal cycling (ratcheting). Otherwise, shakedown occurs, i.e., the imperfection amplitude stops growing.

INTRODUCTION

Thermal barriers are widely used in turbines for propulsion. They comprise a thermally insulating coating having sufficient thickness and durability to sustain an appreciable temperature difference between the load bearing alloy and the surface. Reviews of thermal barrier systems, including their durability and failure modes may be found in [1-6].

There are *four primary constituents* in a thermal barrier system. They comprise (i) the thermal barrier coating (TBC) itself, (ii) the superalloy substrate, (iii) an aluminum containing bond coat (BC) between the substrate and the TBC, and (iv) a thermally grown oxide (TGO) that forms between the TBC and the BC. The TBC is the insulator, the BC provides the oxidation protection and the alloy sustains the structural loads. The TGO is a reaction product. Each of these elements is dynamic and all interact to control the durability. The bond coat emphasized in this study comprises *a Pt-modified diffusion aluminide* [4].

Morphological instability of the thermally grown oxide (TGO) is a dominant failure mode in some thermal barrier systems [6, 8-13]. That is, some initial non-planarities in the TGO grow in amplitude as the system experiences thermal cycling. The growth of the undulation amplitude is associated with crack growth in the TBC, which eventually leads to large scale buckling and failure of the TBC [6]. Five fundamental factors underlie the phenomenon [9]: (1) non-elastic deformation of the bond coat, (2) a growth strain in the TGO due to the oxidation, (3) thermal cycling, (4) an initial imperfection, and (5) thermal expansion misfit between the TGO and the bond coat. The challenge is to understand how these factors interrelate and to derive mechanism-based solutions for the cyclic changes in amplitude. A numerical approach [12] is used to develop a simulation scheme capable of probing a range of mechanistic possibilities. In this paper, *we discuss how some of the fundamental system-parameters effect the development of the morphological instabilities.*

THE MODEL

Previous analyses of amplitude changes upon thermal cycling identified some general requirements and responses, but were limited in the material and geometrical representations [9,10]. In the present analysis, key factors and fundamental understanding of cyclic instability is explored, as some of the material and geometrical limitations are relaxed. In a subsequent study [12], a more comprehensive study regarding effects of material properties are discussed.

The model (ABAQUS) is depicted in Fig 1. It consists of an axi-symmetric undulation in the bond coat with external (periodic) boundaries large enough to assure a negligible interaction between imperfections. The substrate is deep enough to suppress overall bending. Four-node axi-symmetric, bi-linear elements were used. The surface of the TGO facing the TBC is left traction free. (The thermal barrier coating is not present in this study, since its low stiffness is predicted to have a minor effect on the general behavior of the system.) The calculations begin with a thin TGO typical of that found after TBC deposition [4,6,13]. Initially, the structure is stress-free at 1000°C. It is cooled to 0°C and reheated to 1000°C. Once the high temperature is reached, the growth strain is imposed. This sequence is repeated 12 or 24 times (except that the growth strain is not applied in the last half cycle).

Stress relaxation in the TGO is introduced by assigning a yield strength, $\sigma_Y^{tgo} = \pm 1 GPa$ [6,7] at the peak temperature. At all other temperatures, the TGO is regarded as elastic. This protocol assures in stress levels in the TGO consistent with available measurements [4,7]. Introducing a time-dependent relaxation (creep) scheme is deemed inappropriate given the poor fundamental knowledge about the growth strain. Growth of the TGO is simulated by imposing stress-free strains in a user subroutine, *uexpan*. An in-plane component, ε_g, governs the lateral growth, assumed spatially uniform through the thickness. This strain duplicates the formation of new oxide along the grain boundaries of a columnar-grained TGO [6]. Thickening involves a strain normal to the TGO, modeled by adding a strain, ε_t, in the row of TGO elements next to the bond coat. For simplicity $\varepsilon_t = 10\varepsilon_g$, in all of the following calculations.

For all of the present calculations, the undulation size and bond coat thickness have been fixed at a representative size (fig. 1) [4,6,8,13]. Some effects of the initial size have been

	Young's Modulus [GPa]	Poisson Ratio	CTE [ppm°C⁻¹]
TGO	380	0.2	8.4
Bond Coat	190	0.3	14.3
Substrate	190	0.3	14.3

*Figure 1* The geometry and material properties used in the analysis, with the boundary conditions indicated.

Figure 2 (a) Undulation amplitude change over 24 cycles for a range of σ_Y^{bc}, (b) Undulation amplitude change as a function of growth strain, ε_g (12 cycles).

addressed previously, within the context of a ratcheting map [9]. The thermo-elastic properties used are summarized on table I. The substrate is taken to be elastic and the bond coat is assumed to be elastic/perfectly plastic. The growth strain is allowed to vary about the range found experimentally, $10^{-4} < \varepsilon_g < 5 \cdot 10^{-3}$ [13], however, for simplicity of presentation, all of the following results are for a growth strain, $\varepsilon_g = 10^{-3}$.

SIMULATIONS

The change in the undulation amplitude with thermal cycling is displayed in fig. 2. The undulation amplitude either increases with thermal cycling (ratcheting) or stops growing after a few cycles (shake down), fig. 2a. The undulation growth is governed by the growth strain, ε_g (fig. 2b).

Three important parameters influencing morphological instabilities are *the growth strain, the yield strength* of the bond coat and *thermal cycling*. The criticality of the growth strain is visualized by arresting this strain after a few cycles (Fig. 3a). Note that, absent ε_g, the ratcheting stops even though the bond coat and the TGO are allowed to yield. The effects of *temperature*
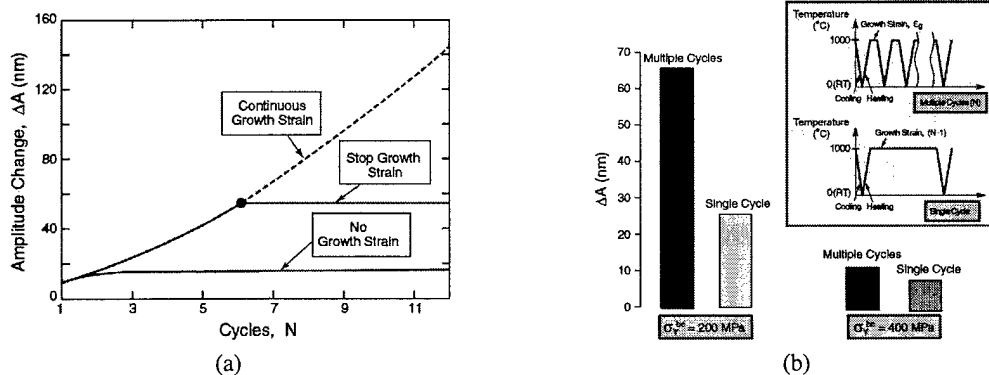
Figure 3 Growth strain and thermal cycling are crucial for undulation amplitude growth. (a) The growth of the undulation amplitude discontinues when the growth strain is absent. (b) Undulation amplitude change for multiple cycles compared to that for a single cycle (for both cases N = 12, thus total growth strain is $11\varepsilon_g$).

M9.4.3

cycling, is demonstrated by comparing the results from cyclic loading to that of the "single-cycle" response. That is, after the first half cycle, the material is held at temperature long enough to accumulate a growth strain, $(N-1)\varepsilon_g$, then cooled to ambient and reheated. The imperfection amplitude that ensues is compared with that obtained after N cycles, each subject to strain, ε_g (except in the final cycle). The results (fig. 3b) indicate that, the cyclic amplitude change is larger than the isothermal, with the difference increasing as σ_Y^{bc} decreases. Similarly, the plastic strains are appreciably smaller after isothermal exposure than upon cycling (not shown). This implies a 'reset' upon cycling, and that plastic straining continues with each thermal cycle. This effect is absent under isothermal conditions.

The importance of *the yield strength* of the bond coat may be explored by tracing the evolution of the plastic zone as well as the associated plastic strains. A synopsis of the plastic zone with thermal cycling is depicted on fig. 4, for two typical yield strengths. A forward plastic zone (cooling) is achieved for both levels of yield strengths (σ_Y^{bc} = 200 and 400 MPa). However, reverse yielding occurs on re-heating only for the case of lower yield strength.

The strains, ε_{pl}, that accumulate within the plastic zone increase systematically with the number of cycles. This is exemplified by the distributions present after 12 cycles (fig. 5a) and by monitoring evolution of the plastic strain where they have a maximum value (fig. 5b). For the case of σ_Y^{bc} = 200 MPa, forward yielding on cooling and reverse yielding on heating occur for each cycle. For a higher yield strength (σ_Y^{bc} = 400MPa), no reverse yielding is achieved and after initial cycling only minor plastic strains occur.

We recall that from figure 3a, lower yield strength results in ratcheting and higher in shakedown. When $\sigma_Y^{bc} < 250MPa$, reverse yielding occurs in the first cycle, whereupon the plastic zone, plastic strain and undulation amplitude change all continue to increase on a cycle-to-cycle basis, with no discernable limit. Conversely, when σ_Y^{bc} is larger, there is no reverse yielding, whereupon the changes in plastic zone size, plastic strain and imperfection amplitude
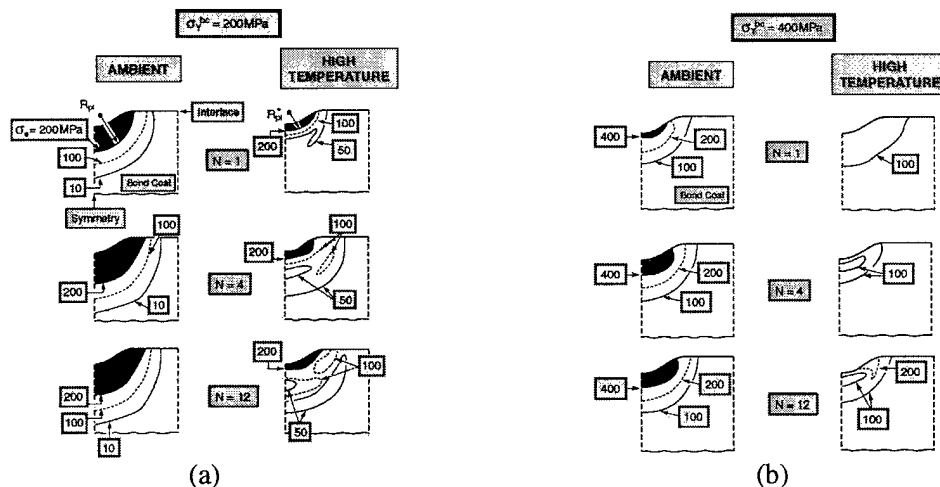

(a)   (b)

Figure 4 A synopsis of the evolution of the stress state in the bond coat over 12 cycles. Stress state at ambient and at peak temperature for (a) σ_Y^{bc} = 200MPa and (b) σ_Y^{bc} = 400MPa.
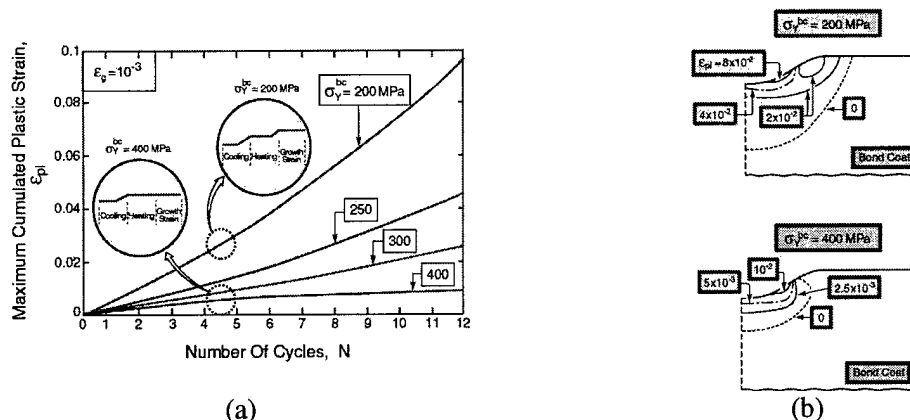
Figure 5 *(a) Evolution of the maximum value of the cumulated plastic strain in the bond coat over 12 cycles. (b) Cumulative plastic strains in the bond coat when $\sigma_Y^{bc} = 200MPa$, and $\sigma_Y^{bc} = 400MPa$.*

decrease significantly or stop after a few cycles. *This yield strength thus appears to represent a bifurcation between ratcheting and shakedown.*

Further understanding is gained by monitoring the stress changes occurring in the TGO at the two levels of σ_Y^{bc} (fig. 6). At the higher σ_Y^{bc} (fig. 6C,D), the stresses become spatially uniform after about 8 cycles and invariant in magnitude with further cycling, indicative of a cyclic "steady-state". Accordingly, after the first few cycles, all subsequent growth strains are "absorbed" by TGO yielding at the peak temperature, accounting for the lack of further changes in plastic zone size and in undulation amplitude. Conversely, at the lower σ_Y^{bc}, spatial variations in the TGO stress persist (fig. 6A,B). This spatial variability is retained as cycling proceeds. Since the TGO is unable to take up the stress-free strain from growth, the bond coat must continue to "absorb" it, resulting in systematic changes in plastic strain and imperfection amplitude.

CONCLUDING REMARKS

A numerical code has been developed and used to simulat morphological instabilities observed in thermally grown oxide, in thermal barrier systems. The simulation included a range of phenomena and constituent properties, such as plasticity in the bond coat, growth strains in the TGO, thermal expansion misfit between the TGO and bond coat, as well as yilding in the TGO at high temperature. The incidence of reverse yielding upon reheating was seen to be a necessary condition for morphological instabilities. That is, whenever the condition for reverse yielding is satisfied during the first cycle, the system ratchets, thus the imperfection amplitude increases. Otherwise, shakedown occurs. For the structure considered, this transition occurs for bond coats having a temperature invariant yield strength of about 250 MPa. That the instability can only occur for "soft" bond coats is inconsistent with the experimental findings [4,13]. Two other effects that expand the ratcheting domain are temperature dependent yield strength a thermal misfit between substrate and bond coat. These effects are therefore investigated in a subsequent study [12].

M9.4.5
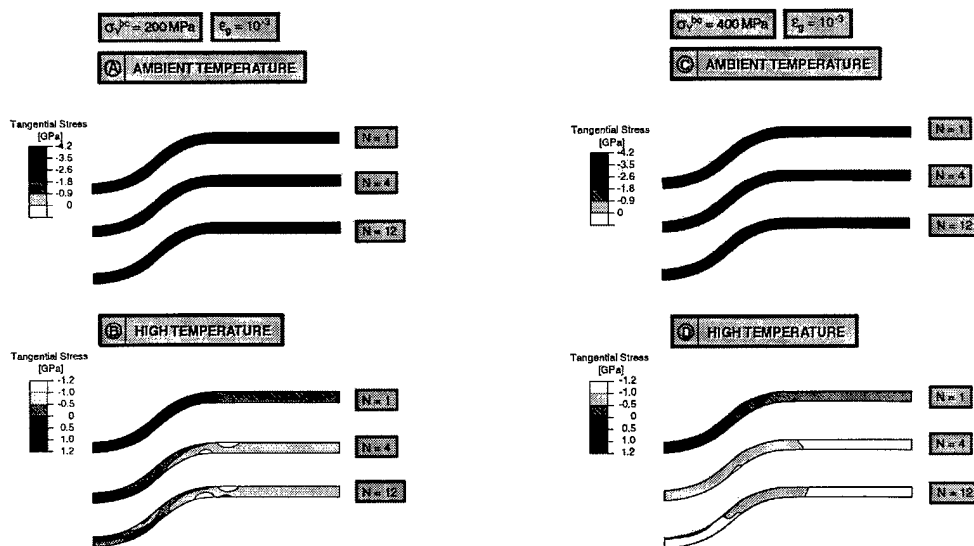
Figure 6 *Evolution of the tangential stress distribution in the TGO upon thermal cycling (first, fourth and twelfth cycle). For $\sigma_Y^{bc} = 200MPa$: (a) ambient temperature, and (b) peak temperature. For $\sigma_Y^{bc} = 400MPa$: (c) ambient temperature, and (d) peak temperature. (Stresses tangential to the TGO/BC interface)*

REFERENCES

1. Miller, R.A., Journal of the American Ceramic Society, **67**, 517 (1984)
2. Strangman, T.E., Thin Solid Films, **127**, 93-105 (1985).
3. Wright, P.K., Evans, A.G., Current opinion in solid state & materials science, **4**, 255-265 (1999)
4. Stiger, M.J., Yanar, N.M., Topping, M.G., Pettit, F.S., and Meier, G.H., Zeitschrift für Metallkunde, **90**, [12], 1069-1078 (1999).
5. DeMasi-Marcin, J.T. and Gupta, D.K., Surface and Coatings Technology, **68/69**, 1 (1994)
6. Evans, A.G., Mumm, D.R., Hutchinson, J.W., Meier, G.H., and Pettit, F.S., Progress in materials science, (2000) in press
7. Tolpygo, V.K., Dryden, J.R., and Clarke, D.R., Acta Materialia, **46**, 927-937 (1998)
8. Tolpygo, V.K. and Clarke, D.R., Acta Materialia, **48**, 3283-3293 (2000)
9. He, M.Y., Evans, A.G., and Hutchinson, J.W., Acta Materialia, **48**, 2593- 2601 (2000).
10. Ambrico, J.M., Begley, M..R., and Jordan, E.H., (2000) submitted for publication.
11. Gell, M, Vaidyanathanm,K., Barber, B., Cheng, J, and Jordan, E., Metallurgical and Materials Transaction A, **30A**, 427-435 (1999).
12. Karlsson, A.M., Evans, A.G., (2000) submitted for publication
13. Mumm, D.R., Spitsberg, I., and Evans, A.G., Acta Mater. (2000) submitted for publication.

Microstructural Characterization of Yttria-Doped Zirconia Coatings with Electron Microprobe Wavelength Dispersive Compositional Mapping

Ryna B. Marinenko, Jennifer R. Verkouteren, and David S. Bright,
National Institute of Standards and Technology, NIST, Surface and Microanalysis Science
Division, Chemical Science and Technology Laboratory Gaithersburg, MD 20899

ABSTRACT

The use of digital electron microprobe x-ray compositional mapping with wavelength dispersive spectrometers to understand the microstructure of yttria stabilized zirconia thermal barrier coatings is described. Data from quantification of element x-ray maps can be utilized to infer what phase or phases are present. Analysis of a plasma-sprayed coating prepared from a fused and crushed feedstock is compared to an annealed specimen of the same material.

INTRODUCTION

For more than a decade, yttria stabilized zirconia (YSZ) thermal barrier coatings (TBCs) have been prepared from feedstocks composed of 0.06-0.08 mass fraction Y_2O_3 stabilized zirconia [1]. The resulting coating is a tetragonal zirconia phase, also called non-transformable or t' zirconia that has the mechanical and thermal stability needed for a good TBC. In service, TBCs are exposed to high temperatures, often above 1100°C, causing phase transformations that result in increased residual stress and eventual spalling. To improve the performance of these TBCs characterization of the microstructure before and after exposure to service conditions is needed. Wavelength dispersive compositional mapping with the electron probe microanalyzer (EPMA) was used to study YSZ TBCs. Phases present in TBCs may be only a few to several micrometers in one or more dimensions; EPMA provides the resolution needed to recognize compositional variations on the micrometer scale. For the YSZ specimens studied here, different phases not visible with an optical microscope or in SEM secondary electron (SE) or backscatter (BS) images became obvious in EPMA digital x-ray element maps. Results of analyses of plasma sprayed coatings prepared from a fused and crushed feedstock are described. Data from quantification of the element maps are used to infer which phases are present.

EXPERIMENTAL

Two specimens of a plasma-sprayed YSZ-TBC were studied. The coating was 4-5 mm thick, purposely prepared for bulk analysis [2] and considerably thicker than industrial coatings that are usually about 300 μm thick. The TBC was prepared from a fused and crushed YSZ feedstock powder with a nominal 0.08 mass fraction of Y_2O_3 (0.087 mole fraction $YO_{1.5}$ or 0.063 Y mass fraction). The stoichiometric phase is $(Zr_{1-x}Y_x)O_{2-x/2}$. One specimen was "as sprayed" and the other was annealed for 1h at 1400°C. Polished cross-sections about 2 cm long and 5 mm wide were coated with 10 nm of carbon. X-ray maps of the cross-sections were acquired with digital beam control in 64 pixel x 64 pixel arrays, a 2-s acquisition time per pixel, at an excitation potential of 25 kV, and a beam current of 50 nA. All maps were 50 μm x 50 μm. From a Monte Carlo calculation [3] the diameter of the sphere from which emitted Y and Zr x-rays were observed was determined to be about 1 μm. Four fixed spectrometers were used for the

simultaneous acquisition of the four x-ray element maps. The yttrium and zirconium Lα lines were mapped with PET crystals while LiF was used for hafnium Lα. The oxygen Kα line was mapped with the LDE1 synthetic multi-layered crystal. Each map was quantified at each pixel using a ZAF (atomic number-absorption-fluorescence) matrix correction procedure, FRAMK, a version of FRAME [4] modified for x-ray mapping, that was developed in this laboratory. Pure element standards were used for the three cations and SiO_2 was used for oxygen. Background corrections were made to each map pixel as well as to standards data. The resulting concentration maps were displayed and evaluated with a Lisp-based imaging program developed in this laboratory [5-7]. Since the mapped area of 50 μm x 50 μm was so much smaller than the bulk coating dimensions (4-5 mm x 2 mm), thirty to forty WDS-EPMA x-ray maps were acquired from each specimen, providing sufficient data to make a valid statistical characterization of the composition of the elements present in the bulk coating. Maps were acquired (most but not all juxtaposed) along a line across the center of each coating cross-section from the interior edge to the external surface. For brevity, only a few of the quantified x-ray element maps, each representative of maps from each specimen, are discussed here. Sources of uncertainties in the mapping data reported here are discussed below.
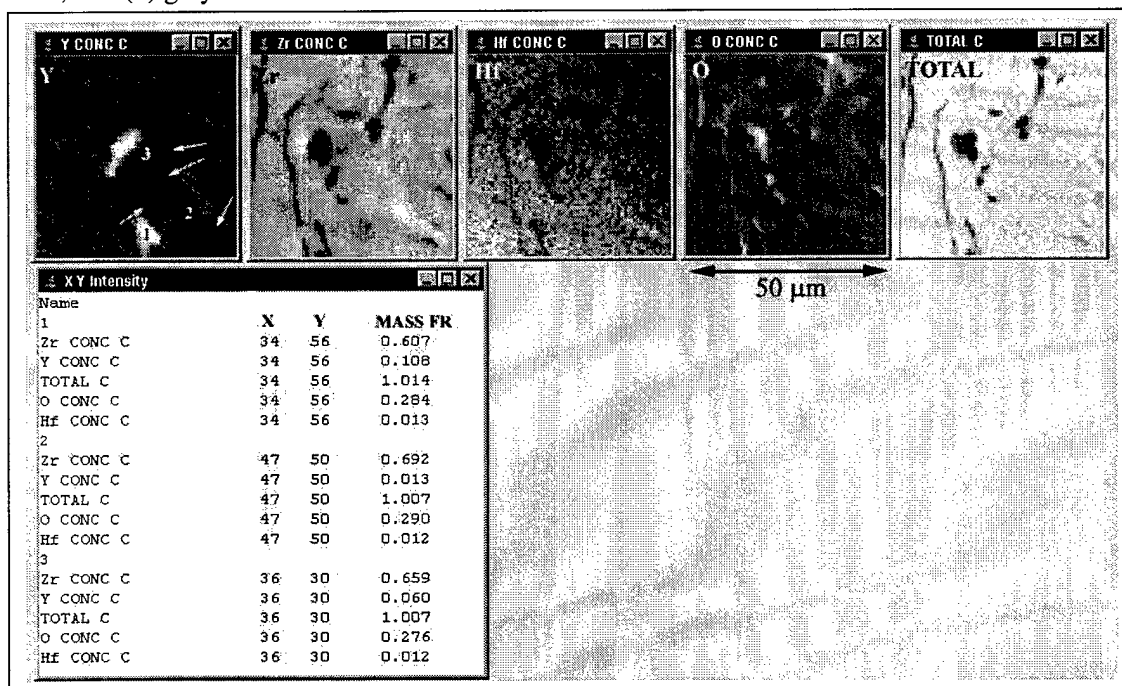
RESULTS

Fig. 1 shows the four individual x-ray element concentration maps, taken simultaneously with four fixed spectrometers. The last map to the right is the analytical Total map or sum of the mass fractions from the corresponding pixels of the four quantified element maps. On the gray level scale, the minimum and maximum concentrations in each element map are black and white, respectively, with intermediate concentrations represented by corresponding levels of gray. When all elements present in a sample are accounted for in the analysis, the Total map to the right should be white except for voids and cracks. The value for most pixels in the Total map should be within a few percent of 1.0 mass fraction. Differences from 1.0 depend on the uncertainty of the analysis and the presence of defocusing [8,9] that is most significant for low magnification maps (dimensions greater that 50 μm on an edge).

The oxygen map has a few bright spots that are due to oxide polishing compounds that occasionally remain in voids or cracks. The bright to dark shading of the cracks in the oxygen map are due to x-ray absorption and geometry, or edge effects, associated with the cracks. The hafnium map is included to complete the mass balance. It is present in small amounts (about 0.015 mass fraction or less) throughout these coatings since it occurs as a natural impurity in Zr. The low statistics of the Hf data in this map are evident from the grainy appearance. There is a slight crystal defocusing that is seen in the change in brightness from the lower left corner to upper right corner of the Hf map. This is not considered a serious contribution to the uncertainty of the quantitative analysis of these maps because the contribution of the Hf to the total mass balance is small.

The Y and Zr maps are most important in these analyses. The bright, white spots in the Y map correspond to a relatively high-concentration Y phase. There are also some dark areas running from top to bottom in the Y map. Some of these dark regions and spots also occur in the Zr, Hf and Total maps; they are probably cracks and voids in the coating. But the larger dark areas (indicated by the arrows in the Y map) that are not obvious in the Zr and Hf maps are a low-concentration Y phase.

M9.7.2

The Lispix software used to study these images can sample individual, selected pixels in one map and simultaneously report the concentration values of corresponding pixels in all element maps in the group. Below the group of maps in Fig. 1 is a table of mass fraction compositions for all five maps taken from the three locations designated in the Y map. The differences in the Y concentration (with corresponding changes in the Zr concentration) from the (1) white, (2) black, and (3) gray areas are evident.


Name	X	Y	MASS FR
1			
Zr CONC C	34	56	0.607
Y CONC C	34	56	0.108
TOTAL C	34	56	1.014
O CONC C	34	56	0.284
Hf CONC C	34	56	0.013
2			
Zr CONC C	47	50	0.692
Y CONC C	47	50	0.013
TOTAL C	47	50	1.007
O CONC C	47	50	0.290
Hf CONC C	47	50	0.012
3			
Zr CONC C	36	30	0.659
Y CONC C	36	30	0.060
TOTAL C	36	30	1.007
O CONC C	36	30	0.276
Hf CONC C	36	30	0.012

Figure 1. Quantified x-ray element maps for Y, Zr, Hf, and O plus the Total map calculated from WDS-EPMA composition map C from the annealed YSZ-TBC specimen. In the table below the maps are corresponding pixel concentrations (in mass fraction) taken from locations 1, 2, and 3 in the Y element map. Arrows in the dark region of the Y map designate the low-concentration Y phase. Columns X and Y specify the coordinates of locations 1, 2, and 3.

Fig. 2 contains two sets of maps (Set A and Set B) each taken from different specimen areas with line profiles for Y and Zr. Set A is from the same area seen in Fig. 1. For set A, the profiles show how the Y and Zr concentrations change along the locus of points (designated by the line in the maps) that traverses through the two white spots and the dark region. The Y concentration (in A) drops from 0.06 mass fraction to less than 0.01 mass fraction and the Zr concentration (in A) increases from about 0.65 mass fraction to about 0.69 mass fraction. A similar change occurs in the Y and Zr concentrations in set B where the locus of points traverses a several-micrometer wide low-concentration Y region to the left of a crack.

Scatter plots of the mass fraction of Y vs. Zr for all pixels from sets A and B above are shown in Fig. 3. In both plots the majority of pixels lie in a concentration region with an average value of about 0.063 mass fraction Y and 0.66 mass fraction Zr, corresponding to the concentration region of the t' phase. The mass fraction for Zr is lower than the stoichiometric

mass fraction of 0.68 in part because Hf that contributes about 0.015 mass fraction is not included.
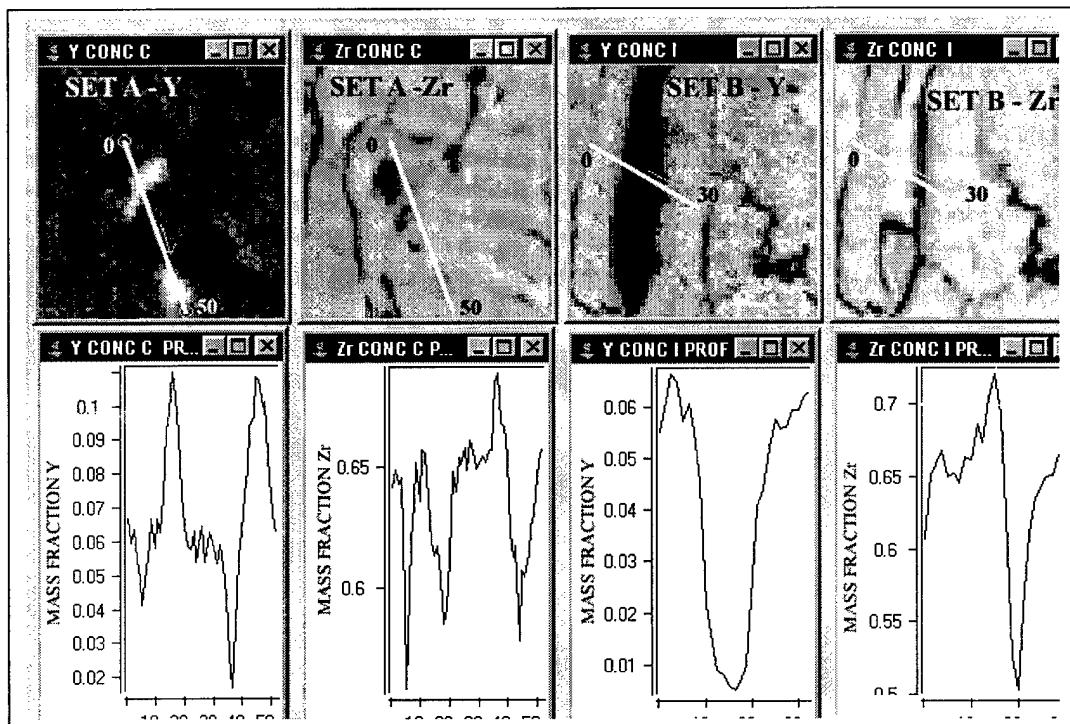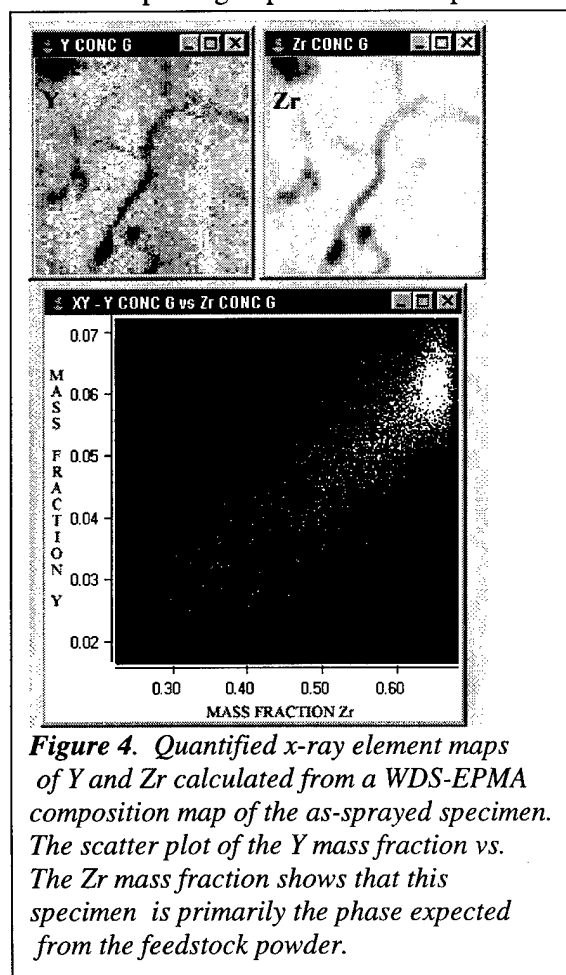

Figure 2. Line profiles showing the Y and Zr concentration changes along the locus of points designated by the white line in each element map. There are two pair of maps, the first for set A and the second for set B, each set from different mapped areas of the annealed specimen.
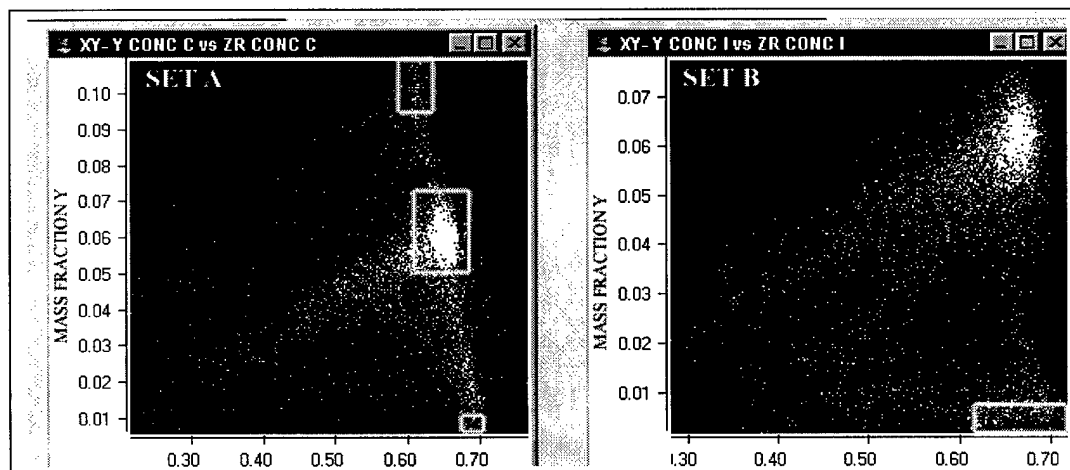
Figure 3. Scatter plots for the Y and Zr maps from set A and B above in fig. 2. These plots provide valuable visual information about the density of the distribution of pixel values (or element concentrations) for the maps they represent.

The points corresponding to the three different concentration regions observed in set A are designated with rectangles. There is a band of points with Y concentrations above (top rectangle) the dominant phase (center rectangle) that correspond to the white spots in the Y element map; in addition there are several points (bottom rectangle) with Y concentrations below that of the dominant phase that correspond to some of the dark, low-concentration Y regions in the element maps. In the scatter plot for set B there are only pixels below the 0.063 mass fraction Y resulting in a "foot" at a concentration <0.01 mass fraction Y. This low-concentration Y phase has been identified by microbeam x-ray diffraction as a tetragonal (t) phase with lattice parameters that are different from the dominant t' phase [10]. The high-concentration Y phase in the set A scatter plot is probably a known cubic phase [11]. The string of pixels that lie between the origin and the high-density points of the dominant phase represent pixels that lie on edges of or on the specimen surface above voids or cracks. Likewise, the band of points above and below those representing the dominant phase represent transition regions on the edges between the high- and low-concentration Y phases and the dominant phase.

Scatter plots can be used to evaluate the area percent of phases present. From either a single element map or a group of element maps from the same specimen, a closed curve can be drawn around a group of pixels to select a concentration region of interest. The number of pixels, average value, and distribution of concentrations within the curve are determined. This information can be used to determine how much of each phase is present. These results were reported by Verkouteren [10] to determine the area percent values from 7 maps of the annealed specimen.

In Fig. 4 are the Y and Zr quantified element maps from a region of the "as sprayed" TBC specimen with the corresponding scatter plot. These maps are representative of all the quantified maps from this specimen. Other than voids and cracks this coating appears to be primarily the composition expected from the feedstock material.

The uncertainty in the concentration data from EPMA x-ray mapping is dependent upon a number of contributing factors that are related to the precision of the x-ray data and the accuracy of the quantification. When time is a factor in mapping, the desired precision at every pixel may be difficult to achieve, especially for elements present at low concentrations (less than 0.05 mass

Figure 4. *Quantified x-ray element maps of Y and Zr calculated from a WDS-EPMA composition map of the as-sprayed specimen. The scatter plot of the Y mass fraction vs. The Zr mass fraction shows that this specimen is primarily the phase expected from the feedstock powder.*

fraction). For example, the total acquisition time for a map of 64 x 64 pixels at 2 s per pixel is about 2.5 h. The time per pixel can be increased, but this will be at the expense of additional data that could be acquired at other sample locations. The disadvantage, though, of lower counting statistics can be outweighed by the increase in the number of data points and maps that contribute to the mapping data set. The uncertainties at the 95% confidence level for Y and Zr that are attributed to the precision of the mapping data acquired in this work are in Table I where

Table I. Single pixel counting statistics (precision) contribution to the experimental mapping uncertainty

	Yttrium		Zirconium	
Phase	Count Rate (cts/pixel/2s)	Uncertainty 2 SD (rel %)	Count Rate (cts/pixel/2s)	Uncertainty 2 SD (rel %)
High Conc. (~0.10 mf Y)	700	7.6		
Dominant (0.063 mf Y)	500	8.9	10,500	2.0
Low Conc. (<0.01 mf Y)	110	19.1		

Table II. Total single pixel uncertainty, 2 SD (rel %), including precision and accuracy (5%) contributions

Phase	Yttrium	Zirconium
High Conc. (~0.10 mf Y)	9.4	
Dominant (0.063 mf Y)	10.3	5.4
Low Conc. (<0.01 mf Y)	19.6	

the average count rates per 2s and the 2 standard deviation (2 SD) contributions in relative percent are listed. There is a distinct difference in count rates for Y between the high (white spots), median (or dominant), and low concentration regions. Three different concentration regions are discernable in the data from these maps with no overlap of the uncertainties due to counting precision. For Zr, the precision does not change significantly from one phase to the next because of the high concentration and resulting high count rate for this element. The effect of the relative difference in the precision between the two elements can be seen in the scatter diagrams (Figs 3 and 4). The density of pixels representing the dominant phase in the coating forms an ellipse with the long axis in the y-direction, or along the axis of the" Mass Fraction Y" where the greatest uncertainty due to precision occurs.

The accuracy of quantitative EPMA results is usually estimated from experience since many factors, such as absorption coefficients, stopping power, backscatter electron coefficients, etc. play a role in the correction procedures. Depending upon the elements present, some of these parameters are well known while others are poorly known. They also depend upon the excitation voltage used, and that voltage may not be favorable for all elements in the sample. Standards and background data must also be carefully chosen and analyzed. A conservative estimate for the accuracy is generally 5% relative at 95% confidence for quantification using element standards, but for many analyses this estimate is too high. Even if a 5% relative accuracy is added in quadrature to the precision errors cited above to obtain an estimate of the total uncertainty as shown in Table II, three distinct concentration regions for YSZ would exist with still no overlap in the uncertainties from one region to the next.

In addition, two factors strongly support the accuracy of the quantitative results cited in the discussions above and support the fact that the accuracy, particularly for Y and Zr, is better than the 5% relative estimate mentioned in the previous paragraph. Firstly, the concentration of the 0.063 mass fraction Y in the dominant phase of the coating, especially in the "as sprayed" coating specimen is in agreement with the concentration expected for this phase from the original feedstock powder composition. This gives significant validity to the experimental parameters used in the mapping procedure and the quantification of the maps. Secondly, in the analytical Total maps, such as the one shown in Fig. 1, that are the sum of corresponding pixels from the four quantified element maps, the pixel values are 1.0 mass fraction with an uncertainty of about 0.03 mass fraction or less for pixels that are not on edges of cracks or voids; i.e., the total mass is close to 100 percent.

CONCLUSION

Quantitative compositional mapping with EPMA is a valuable technique for understanding the element distributions of plasma-sprayed YSZ TBCs on the micrometer scale. Element concentration maps were used to evaluate the extent of microheterogeneity, to help predict what phases were present, and to locate regions of interest that were not obvious in an optical microscope or in a SEM secondary or backscatter electron image. The technique was successfully used here to locate regions for further analyses where the annealing process had caused compositional changes in the coating. Uncertainty calculations and estimates support observations that both high- and low-concentration Y phases result from the annealing of the "as sprayed" specimen.

REFERENCES

1. P. Scardi, M. Leoni, and L. Bertamini, *Surface and Coatings Technology*, **76-77**, 106-112 (1995).
2. J. Ilavsky and J. K. Stalick, *Surface and Coatings Technology*, **127**, 120-129 (2000).
3. J. T. Armstrong, *Inst. Phys. Conf. Proc. Ser. No 165*, Proc of the 2nd Conf. Internat. Union of Microbeam Analy. Socs., Hawaii, July 2000 (Inst. Phys. Pub., Phila. PA)
4. H. Yakowitz, R L Myklebust, and K. F. J. Heinrich, FRAME: an on-line correction procedure for quantitative electron probe microanalysis. *Nat. Bur. Stand. (U. S.) Tech. Note 796*, 46 p. (1973).
5. D. S. Bright, *Microbeam Analysis*, **4**, pp.151-163 (1995).
6. D. S. Bright, *Microscopy and Microanalysis*, **6** suppl. 2, pp. 1022-3 (2000).
7. D. S. Bright, *Microscopy and Microanalysis*, **6** suppl. 2, pp. 1056-7 (2000). See web site www.nist.gov/lispix/.
8. R. B. Marinenko, R. L. Myklebust, D. S. Bright, and D. E. Newbury, *J. Microscopy*, **145**, pt.2, 207-23 (1987).
9. R. B. Marinenko, R. L. Myklebust, D. S. Bright, and D. E. Newbury, *J. Microsc.*, **155**, pt 2, (1989).
10. J. R. Verkouteren, R. B. Marinenko, D. S. Bright, this volume.
11. M. Yashima, M. Kakihana, and M Yoshimura, *Solid State Ionics*, **86-88**, pp. 1131-49 (1996).

CHANGES IN CRYSTAL STRUCTURE AND MICROHARDNESS DURING THERMAL TREATMENT OF A NiCoCrAlY ALLOY.

Thomas Rehfeldt*, Gerhard Schumacher** and Hellmuth Klingelhoeffer**

*Hahn-Meitner-Institut Berlin GmbH, Glienicker Strasse 100, D-14109 Berlin, Germany;
**Bundesanstalt fuer Materialforschung und -pruefung, Unter den Eichen 87, D-12205
Berlin, Germany

ABSTRACT

The stability of microstructure and the microhardness of a NiCoCrAlY alloy was studied after thermal treatment at high temperatures and subsequent quenching into ice water. The alloy revealed mainly two ordered phases, a γ' phase with $L1_2$ crystal structure and a β phase with B2 structure. The γ' phase is shown to become unstable in the temperature range between 1073 K and 1373 K where it undergoes an order-disorder phase transformation. The low transformation temperature compared to pure Ni_3Al is ascribed to deviations from the Ni_3Al stoichiometry and to the additional alloying elements Co and Cr. The γ'-γ order-disorder transformation is shown to be attended by a decrease in microhardness of about 30 %.

INTRODUCTION

For the further increase of temperature in the combustion chambers of gas turbines thermal barrier coatings (TBC) on turbine blades are presently being tested. Due to the different thermal expansion coefficients of superalloy and TBC large stresses are induced at the metal – ceramic interface. In order to reduce these stresses, bond coat alloys are deposited between the superalloy and the TBC. High plasticity of the bond coat alloys is, therefore, required in order to adapt the stresses induced by the different thermal expansion coefficients of superalloy and TBC. The high porosity of the TBC also requires protection of the superalloy by the bond coat alloy against oxidation.

NiCoCrAlY alloys are candidate materials for application as bond coat material deposited between superalloys and ceramic TBCs on turbine blades [1,2,3]. Some NiCoCrAlY alloys were shown to exhibit changes in the coefficient of thermal expansion at high temperatures which are poorly understood [3,4]. The microstructure of such NiCoCrAlY alloys generally consist of mainly two phases, a γ' phase with ordered $L1_2$ crystal structure (Cu_3Au type structure) and a β phase with ordered B2 crystal structure (CsCl type structure). Many ordered alloys are, however, known to become unstable at high temperatures and transform into the corresponding disordered phase leading to large changes in heat flow near the phase transition temperature and, therefore, to large changes in thermal expansion [5].

This work presents results of investigation of microstructure and microhardness of a NiCoCrAlY alloy at high temperature. The composition of the alloy (see Table 1) is close to the ones investigated by Clemens and coworkers [3] and by Brindley [4].

EXPERIMENTAL

Microstructure was examined by means of a scanning electron microscope (SEM) at 30 kV and by means of a transmission electron microscope (TEM) at 120 kV and 300 kV. The composition of the phases was measured by means of energy dispersive X-ray spectroscopy (EDXS) in SEM and in TEM (see Table 1). The structure of the phases was determined by means of selected area electron diffraction (SAED) in TEM. For each condition, at least four different grains were analyzed. In order to determine the crystal structure uniquely, diffraction patterns were recorded along different crystallographic directions.

Table 1: Composition (in at %) of the γ' and β alloy and of the three phases in NiCoCrAlY bond coat alloy. As a comparison, the nominal composition of the bond coat alloy is added.

	Ni	Cr	Co	Al	Si	Hf	Y
Nominal composition of bond coat alloy	42.11	16.51	18.0	22.46	0.54	0.04	0.34
β phase in the bondcoat alloy*	45	8	14	31	1	1	0
β phase in the bondcoat alloy**	41	12	15	29	1	0	2
β alloy**	44	7	13	34	1	0	1
γ' phase in the bondcoat alloy*	36	26	24	12	1	1	0
γ' phase in the bondcoat alloy**	37	23	24	14	1	0	1
γ' alloy**	34	27	26	11	1	0	1
Cr-rich phase in the bondcoat alloy*	16	68	9	5	2	0	0

* measured by means of TEM/EDXS;   ** measured by means of SEM/EDXS

Specimens for investigation by means of TEM were produced by polishing the material mechanically to a thickness of about 100 μm. Discs of 3 mm diameter were punched from these slices. The discs were electrochemically thinned at 253 K in a TENUPOL using an electrolyte which consisted of 10 % perchloric acid, 90% ethanol and 7g Thiourea per dm^3 electrolyte.

The γ' and the β alloys were produced by melting together the elements in a high frequency induction furnace. After the melting process the furnace was switched off and the alloy cooled down to room temperature under non-defined conditions in the furnace. While part of the material was kept in the as-received condition, other parts were subjected to heat treatment at high temperature (see Table 2). For the heat treatments the material was encapsulated in quartz ampoules under argon atmosphere (partial pressure: 250 ± 10 mbar). During the heat treatment the temperature was controlled by means of a thermocouple fixed in the furnace with an accuracy of about 5 K. After heat treatment the capsules were removed from the furnace and put into a water basin where the glass capsule was destroyed immediately. The quenching rate of the material obtained by this procedure is estimated to be about 300 K/s.

The Vickers hardness of the β phase was measured using an applied load of 0.245 N while all specimens of the γ'phase were measured with both 0.245 N and 2.0 N. For each specimen at least 10 indentations were elevated.

Table 2: Ageing conditions prior to water quenching

	Ageing temperature [K]	Ageing time [h]
NiCoCrAlY – alloy	1073	24
	1373	3
γ' - alloy	1073	24
	1173	16
	1273	10
	1373	3
β - alloy	753	120
	923	24

RESULTS AND DISCUSSION

The compositions of the γ' and the β alloy are listed in Table 1. As a comparison the compositions of the three phases detected in the NiCoCrAlY alloy are listed in Table 1. The difference in composition between the phases in the NiCoCrAlY alloy and the corresponding single phase alloys are ascribed to uncertainties in weighing the element powders, uncertainties in the EDXS measurements and due to weight losses during melting.

Fig. 1 shows the SAED patterns recorded in the γ' and β phase of the NiCoCrAlY bond coat alloy and in the γ' alloy after heat treatment and subsequent quenching into water. The SAED patterns of the γ' phase in the NiCoCrAlY alloy reveals superlattice reflections (SLR) labeled by arrows in Fig. 1 in the initial state and after quenching from 1073 K while the SAED pattern of the specimens quenched from 1373 K does not reveal SLRs. The presence and lack of SLRs in the SAED patterns indicates the presence and lack, respectively, of a certain degree of long-range order (LRO) in the alloy. The presence of SLRs in the SAED pattern of the as-produced specimen and in the specimens quenched from 1373 K, therefore, suggests that the γ' phase transformed into the disordered γ fcc solid solution phase in the temperature range between 1073 K and 1373 K. Accordingly, the same kind of phase transformation occurs in the γ' alloy between 1073 K and 1173 K. The order-disorder transformation in both the γ' phase of the NiCoCrAlY alloy and in the γ' alloy takes place at about the same temperature.

The SAED patterns of the β phase reveals SLRs under all conditions. This indicates that even after quenching from 1373 K a certain degree of LRO is present. This does not necessarily mean that the β phase is stable at very high temperatures. Due to its simple crystal structure ordering is very fast and possible disorder at high temperatures cannot be frozen-in by rapid quenching. This phenomenon is well-known from the Cu-Zn alloy which at room temperature has also B2 structure and which undergoes an order–disorder transformation at about 723 K [6]. Even by very fast quenching from high temperatures it is not possible to freeze the disordered structure of Cu-Zn [6].

The critical temperature T_c of the γ'-γ phase transformation is small compared to that of Ni_3Al which lies near the melting temperature of 1908 K of Ni_3Al [7]. This low value of T_c is ascribed to the deviation from stoichiometric Ni_3Al, that is, additions of Cr and Co and lower amounts of Al serve to lower T_c. The interpretation of the decrease in T_c by the addition of ternary and quaternary elements is supported by the results of Masahashi and coworkers [8] who investigated the thermal stability of the γ'-phase in $(Ni_{(1-x)},Fe_x)_3$ Al alloys as a function of

the iron concentration x and found that T_c decreases by about 600 K due to the addition of only 5 at% Fe. The interpreation of our results in terms of a phase transformation is supported by the ternary phase diagram of the Ni-Al-Cr system [9]. According to this phase diagram a NiCrAl alloy which has the same Al and Cr content as our γ' phase lies at 1123 K in the γ' phase field whereas at 1273 K it lies in the γ phase field.
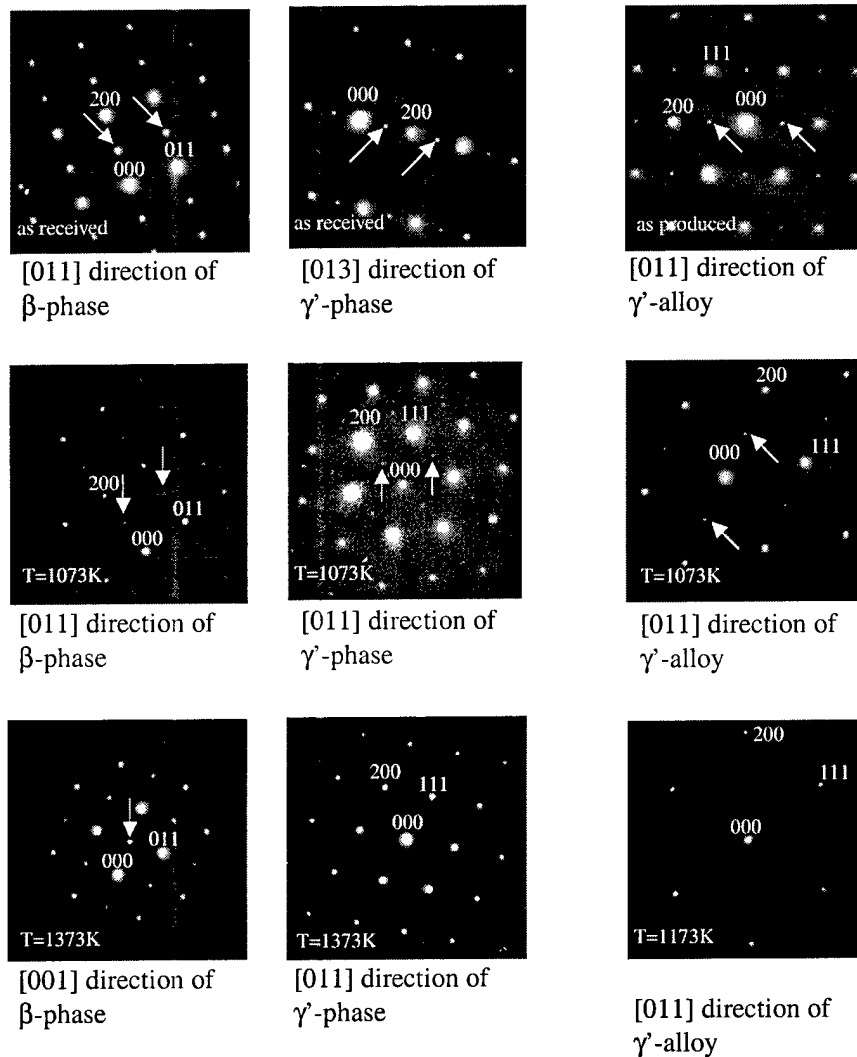

[011] direction of β-phase	[013] direction of γ'-phase	[011] direction of γ'-alloy

[011] direction of β-phase	[011] direction of γ'-phase	[011] direction of γ'-alloy

[001] direction of β-phase	[011] direction of γ'-phase	[011] direction of γ'-alloy

Fig. 1: SAED pattern of β- and γ'-phase and of the γ'-alloy in the as received condition and after quenching from high temperatures

Fig. 2 shows the microhardness as a function of the ageing temperature. The microhardness of the γ' – and γ-phase is smaller than the microhardness of the β-phase under all conditions. The microhardness of the γ' alloy increases by annealing at 1073K/24h and decreases by ageing above 1073K. If we assume that a decrease in LRO correlates with a decrease in microhardness, the increase in microhardness by ageing at 1073K is assigned to an increase in LRO. The correlation between LRO and microhardness might be due to changes in the atomic bondings and/or due to a decrease in the relative amount of antiphase boundaries which cause

elastic strain fields and may serve as obstacles for the movement of dislocations because the burgers vectors of dislocations in the ordered and disordered phases are different. Additionally, the ordered state may obtain a smaller amount of slip systems compared to the disordered state. After melting together the elements to produce the γ' alloy, the furnace is switched off and the alloy cooled down slowly under non-defined conditions. During the cooling process a certain degree of LRO is established. The equilibrium degree of LRO for room temperature is, however, not achieved due to the small atomic mobility at low temperatures. At 1073K the mobility of atoms is high enough to establish the corresponding equilibrium degree of LRO.

Fig. 3 shows the microhardness at 1073K as a function of ageing time. The micograph shows that the microhardness obeys a logarithmic law. The microhardness, therfore, increases steeply in the first few hours while after about 5 hours the changes in microhardnes are relatively small. This behaviour confirms that the LRO was not achieved after cooling the alloy down to room temperature in the furnace but approaches the equilibrium state after ageing at 1073K for 12 hours.
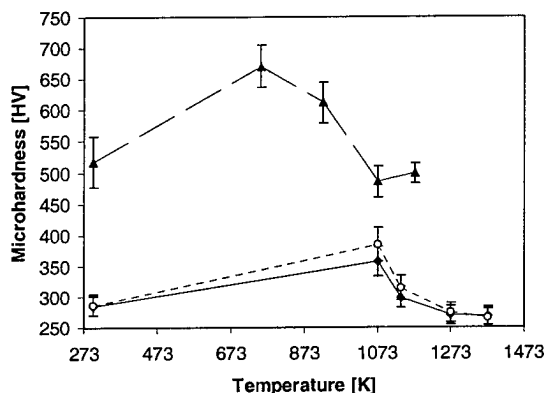

Fig. 2: Microhardness of γ'- and β- alloy as a function of ageing temperature. The open circles and the solid squares denote measurements in the γ'-alloy while solid triangles denote measurements in the β-alloy.
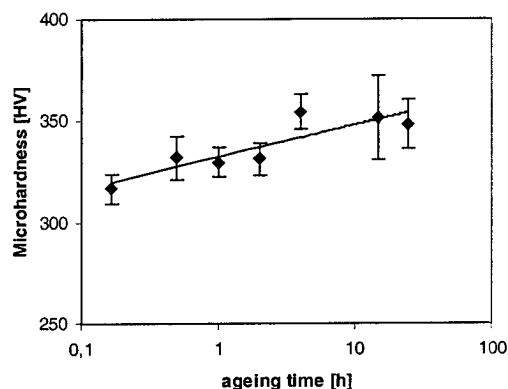
Fig. 3: Microhardness of γ' alloy at 1073 K as a function of ageing time. The error bars indicate the standard deviation.

The decrease in hardness of γ' phase above 1073 K is ascribed to the decrease in LRO at the critical temperature for phase transformation. Within the experimental uncertainty, the microhardness attains the same value after ageing at 1173 K as it attained after furnace cooling and it decreases further by ageing at 1273°C. While SLRs indicated a certain degree of LRO after furnace cooling, there were no SLRs indicating any LRO after ageing at 1173 K. One would, therefore, expect a lower value of microhardness after ageing at 1173 K than after furnace cooling. The relatively high value of the microhardness at 1173 K may be due to the presence of short-range order (SRO) at temperatures slightly above T_c as is known for many alloys (see, e.g., ref. [6] or ref. [10]).

The results of the present work are in qualitative agreement with the results of Noguchi and coworkers [11] who measured the microhardness in a NiCoCrAlY alloy after ageing at high temperatures and subsequent quenching into ice water. They found a decrease in microhardness of about 15 % at about 1273 K which they assigned to homogenization of the material, i.e., to the transformation of the γ' phase into γ-phase. Furthermore, Tawancy [12]

measured the 0.2 % yield strength and ultimate tensile strength of a NiCrMn alloy which at room temperature is strengthened by ordered $Ni_2(Cr,Mo)$ precipitates. Ageing for 8000h at 810 K resulted in a dissolution of the ordered domains and to a decrease in yield strength and tensile strength by about a factor of 2 and 1.5, respectively. Heermant [13] listed the hardness and yield strength of many metallic systems and found a linear correlation between the two parameters. A decrease in yield strength due to order-disorder transformation can, therefore, be concluded from the measurements in microhardness.

SUMMARY AND CONCLUSIONS

The stability of γ' and β phase in a NiCoCrAlY bond coat alloy was studied by means of TEM/SAED. An order-disorder transformation was revealed in the γ' alloy in the temperature range 1073 K to 1273 K. This transformation temperature is low compared to pure Ni_3Al for which a critical temperature for phase transformation of 1883 K is reported in literature. This low temperature for phase transformation is ascribed to the additional alloying elements Co and Cr which are supposed to lower the critical temperature in analogy to the lowering of T_c of Ni_3Al by Fe [8]. The order-disorder transformation is accompanied by a decrease in microhardness by about 30%. This decrease in microhardness is ascribed to differences in the atomic bondings, burgers vectors, slip systems and mass densitys of the ordered and disordered state. The decrease in microhardness of the phase is expected to be related with a decrease in yield strength. Bond coat materials with lower Cr and Co content and higher Al content are, therfore, expected to posses a higher order-disorder transformation temperature. The yield strength for such alloys is expected to drop down at higher temperatures than for the alloys investigated in the present study.

ACKNOWLEDGEMENT

REFERENCES

[1] C. Mennicke, D. R. Mumm and D. R. Clarke, Z. Metallkd. 90, 1079 (1999)
[2] M..J. Stiger, N.M. Yanar, M.G. Topping, F.S. Pettit and G.H. Meier, Z. Metallkd. 90, 12 (1999)
[3] D. Clemens, R. Munoz-Arroyo and W.J. Quaddakkers, in: "Innovative Materials Systems to Increase the Efficiency of Stationary and Air Craft Gas Turbines" , Workshop, 17.02.2000, DLR, Köln, Germany (2000)
[4] W.J. Brindley, Journal of Spray Technology 6, 85 (1985)
[5] K. Mitsui, Y. Mishima and T. Suzuki, Phil. Mag. B 53, 447 (1986)
[6] D.A. Porter and K.E. Easterling, "Phase Transformations in Metals and Alloys", Chapman & Hall, 365 (1992)
[7] K. Mitsui, Y. Mishima and T. Suzuki, Phil. Mag. B 62, 395 (1990)
[8] N. Masahashi, H. Kawazoe, T. Takasugi, O. Izumi, Z. Metallkde 78, 788 (1987)
[9] P. Villars, A. Prince, and H. Okamoto, Handbook of Ternary Alloy Phase Diagrams, ASM International (1995)
[10] A. Marucco and B. Nath, J. Mater. Sci. 23, 2107 (1988)
[11] K. Noguchi, M. Nishida, A. Chiba, J. Takeuchi and Y. Harada, Proc. of ITSC95, Kobe, 459 (1995)
[12] H.M. Tawancy, Metall. Trans. 11 A, 1764 (1980)
[13] C. Heermant, PhD Thesis, Berlin, 1998

In-Plane Cracking Behavior Near and Away From Interface of Thermal Barrier Coatings and Thermally Grown Oxides

Z. Zhang*, J. Kameda*[#], A. H. Swanson* and S. Sakurai[$]
*Ames Laboratory, Iowa State University, Ames IA, USA
[#]Office of Naval Research International Field Office, Tokyo, Japan
[$]Mechanical Engineering Research Laboratory, Hitachi Ltd., Hitachi, Japan

ABSTRACT

The initiation characteristics of in-plane cracks near and away from the interface of thermal barrier coatings (TBC) and thermally grown oxides (TGO) have been studied using a protruded four-point bend testing technique together with a finite element analysis. In-plane TBC cracks were initiated near and away from the TBC/TGO interface, respectively, in protruded specimens without and with grooved substrates. It was shown that the onset of in-plane TBC cracks near or away from the interface in the protruded TBC tests was controlled by the out-of-plane tensile stress but not by the principal tensile stress acting upon an inclined plane to the interface. The critical local tensile stress for the initiation of TBC cracks near the interface was found to be 20% lower than that away from the interface. The TBC cracking near and away from the TBC/TGO interface is discussed in light of the residual stress distribution through the TBC thickness.

INTRODUCTION

Thermal barrier coatings (TBC), made up of Y_2O_3 stabilized ZrO_2, (YSZ), and metallic bond coatings (BC) commonly have been applied by a plasma spraying (PS) method to protect hot-section components in aerospace and land-based gas turbines. It is recognized [1-3] that TBC processed by the PS method delaminates while in-service under thermal/mechanical stress cycles as a result of in-plane cracking in TBC adjacent to the TBC/BC interface. There are two major reasons for the TBC delamination. First, the build-up of residual stresses occurs during thermal cycling due to the difference in the thermal expansion coefficient between TBC and BC/ substrate. Secondly, high oxygen permeability of YSZ results in the formation of thermally grown oxide (TGO), made up of alumina, near the TBC/BC interface. In order to maintain the integrity of advanced gas turbines and to develop better TBC systems, it is necessary to examine the characteristics of TBC delamination induced while in-service. For this purpose, several mechanical testing methods, such as notched bending test [4], pull test [5], and protruded compressive test [6] have been carried out. Yet, the mechanisms of TBC delamination, such as the effects of the residual stress and TGO, have not been fully understood, due to lack of experiments controlling the in-plane TBC cracking and detailed mechanistic analysis.

In this paper, in-plane TBC cracking behavior is studied using a protruded four-point bend testing method recently developed [7-10]. Different features of TBC cracking near and away from the TBC/BC interface are shown using protruded TBC specimens without and with grooved substrates. By applying a finite element method (FEM), the critical local tensile stress is determined for the crack initiation near and away from the TBC/TGO interface. The effect of the residual stress distributed in the TBC on the near- and away-from-interface TBC cracking is discussed.

EXPERIMENTS AND MATERIALS

The material used in this study was taken from a transition duct section of a gas turbine combustor, operated for 18,451 hours with thermal cycles of 461 under liquefied natural gas fuel. TBC (6% Y_2O_3 stabilized ZrO_2) and BC (40.1at.%Ni-20at.%Co-16.5at.%Cr-23at.%Al-0.2at.%Y) had been deposited over a Ni-based superalloy (Nimonic 263) using an atmospheric

PS method. Figure 1 shows scanning electron micrograph of the TBC/BC system studied. The thickness of the TBC and BC were 285 and 40 μm. Based on scanning Auger microprobe analysis, it was found that a wavy TGO layer with the thickness of 15 μm had formed near the TBC/BC interface due to in-service environmental attack (Fig. 1).

Protruded specimens were machined from the transition duct. In order to produce a stress concentration effect near the TBC/ TGO interface, TBC was protruded from the substrate by machining both the TBC ends of a thin plate using a grinding machine. By optical microscopy observation on the side surfaces of protruded specimens, it was confirmed that the lower end of a root radius (ρ = 0.2 mm) at the protruded TBC edge was located at or between the TGO/BC and BC/substrate interface. In a protruded TBC specimen without reinforcement, it was shown [7,8] that near-interface cracks did not form due to the extension of pre-existing out-of-plane cracks and lower stress intensification at the protruded edge. Thus, reinforcement made of a titanium alloy sheet (0.6 mm thick) was attached on the top of the protruded TBC using an adhesive (3M EC2214) with the thickness of 0.08-0.15mm. In addition, protruded TBC specimens with grooved substrates (0.6 mm deep) were prepared to enhance the local stress at the root radius. The geometry of ungrooved and grooved protruded specimens with the substrate thickness of 1.2 mm and four-point bending spans used in the present study are shown in Fig 2.

Protruded four-point bending tests were carried out at room temperature using a screw-driven Instron testing machine with the crosshead speed of 6.4 x 10^{-6} m/s. The load vs. deflection curve was monitored and stored via a computer. The morphology of TBC cracking in load-interrupted protruded TBC specimens was examined by optical microscopy.

EXPERIMENTAL RESULTS

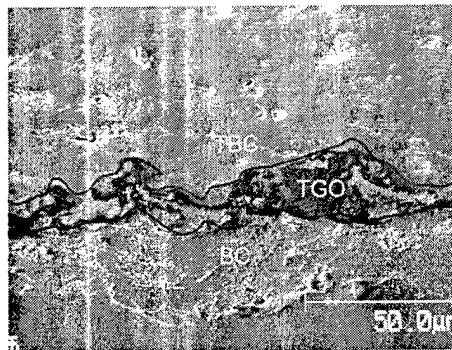Figure 3 indicates the typical load vs. deflection curves obtained from tests on protruded

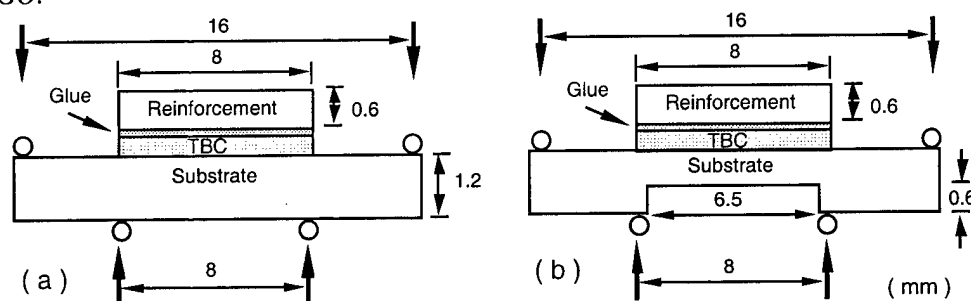*Figure 1. Secondary image micrograph near the TBC/BC interface indicating formation of wavy TGO.*

Figure 2. Geometry of protruded TBC four-point bending specimens (a) without and (b) with grooved substrate and the supporting and loading spans.

TBC specimens without and with the grooved substrate. The loading rate was found to change at a critical load (P_c). In order to examine if P_c represents the TBC crack initiation near the root radius, a protruded specimen was load-interrupted just prior to and after P_c (BO1 specimen in Fig 3). It was shown [8] that in-plane TBC cracking took place in a protruded specimen interrupted just above P_c, but not below P_c. In grooved protruded specimens tested, the compliance change was immediately followed by the maximum load (CNS1 specimen in Fig. 3). We can see quite different values of P_c between the ungrooved and grooved specimen tests. As shown in Fig. 4, different characteristics of the TBC cracking were observed in the two types of protruded specimen tests. In-plane TBC cracks were initiated near and away from the TBC/TGO interface, respectively, in the protruded specimens without and with the grooved substrate.

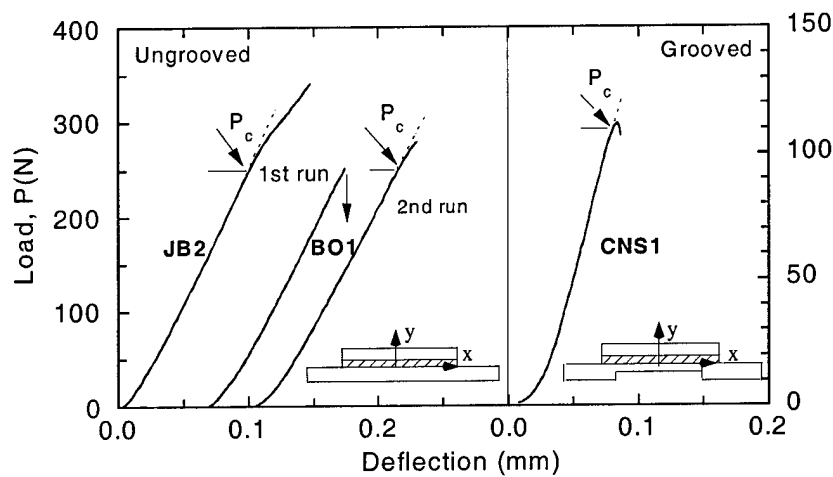## CRITICAL LOCAL TENSILE STRESS FOR IN-PLANE TBC CRACKING

Figure 3. Load vs. deflection curves obtained from bending tests on protruded TBC specimen (a) without and (b) with grooved substrate. The specimen (BO1) was load-interrupted just before and after P_c ,defined as the critical load for crack initiation.
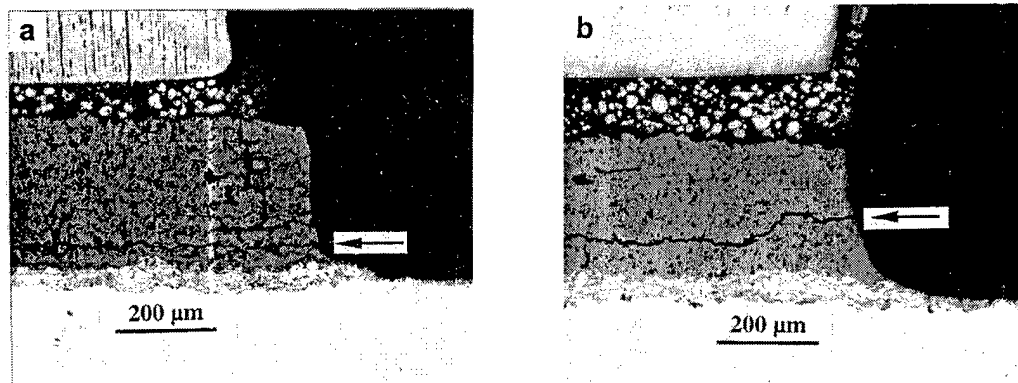

Figure 4. Morphology of TBC cracking (a) near and (b) away from the TBC/TGO interface in protruded TBC specimens without and with grooved substrate (BO1 and CNS1). Arrows indicate the crack initiation site.

In an effort to analyze the TBC delamination behavior in the protruded TBC test, FEM stress analysis was performed using ANSYS code. The protruded TBC specimen tested was considered as a layered structure with different elastic moduli (E). The layers consist of the reinforcement (E = 120 GPa), adhesive (E = 5 GPa), TBC (E =40 GPa), TGO (E = 400 GPa), BC (E = 200GPa), and substrate (E = 210 GPa). The elastic moduli of the TBC and adhesive were determined from four-point bending tests on coating specimens, which had been extracted chemically from the substrate, and tensile tests on molded adhesive samples. The FEM mesh scheme was created using ANSYS GUI. The detailed mesh and the elastic-plastic properties (Poisson's ratio and yield stress) of the adhesive, BC and substrate are shown elsewhere [10]. In the present FEM analysis, the x- and y-axis correspond to the longitudinal (in-plane) and transverse (out-of-plane) directions of the protruded TBC specimen. FEM stress analysis was carried out at the nominal bending stress (σ_n) = 366 MPa, which was defined as the maximum bending stress in the substrate (1.2 mm thick).

The distributions of the in-plane and out-of-plane tensile stresses $(\sigma_{xx}$ and $\sigma_{yy})$, the shear stress (τ_{xy}), and the principal tensile stress (σ_p) were determined along the contour of a root radius in the protruded TBC specimens. Several important features were summarized [10,11]: (i) the peak of out-of-plane σ_{yy} appeared further away from the lower end of the root radius than that of the other stress components; (ii) the value of σ_p, acting upon an inclined plane to the interface, was much larger than that of σ_{yy} while they converged with each other with increasing the y distance; (iii) the local stress distribution in the TBC almost remained the same regardless of whether the TGO is present or not.

As shown in Fig. 4, the TBC crack growth occurred not along the inclined plane, where σ_p is operative, but almost parallel to the interface. Hence, the TBC cracking is not controlled by σ_p but by σ_{yy}. The distributions of σ_{yy}, normalized by σ_n, are shown along the contour of a root radius in the protruded specimens with the ungrooved and grooved substrate in Fig. 5. Machining a groove into the substrate enhanced the stress intensity and caused the position of σ_{yy}^{m} (the maximum value of σ_{yy}) to shift slightly further away from the interface. Taking into account the TBC crack initiation site in the local stress distribution (indicated by arrows in Figs. 5), we can estimate the critical local tensile stress (σ^*) controlling the initiation of TBC cracks near and away from the TBC/TGO interface. It is evident in the ungrooved protruded specimen that the TBC crack near the interface was initiated at y_c =0.08 mm, which was not at the position of σ_{yy}^{m}. On the other hand, the TBC cracking away from the interface occurred near
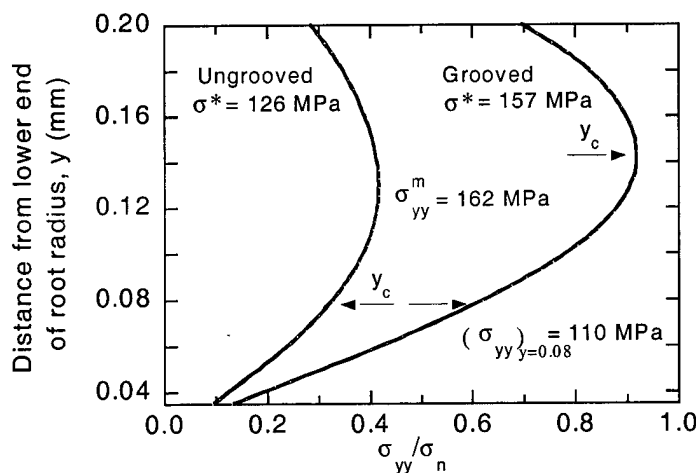

Figure 5. Comparison of distribution of out-of-plane tensile stress (σ_{yy}) normalized by σ_n along the contour of root radius in protruded TBC specimen without and with grooved substrate.

σ_{yy}^m in the grooved specimens tested. The average values of σ^* for the TBC cracking near and away from the TBC/TGO interface were found to be 126 MPa and 157 MPa, respectively, which was determined from each three samples without and with the grooved substrate. That is, in-plane TBC cracks more readily formed near the interface than away from the interface.

DISCUSSION

It is interesting to note that the presence of a groove in the substrate affects the site of in-plane TBC cracking and the critical local tensile stress for the TBC cracking in the protruded specimen tests. In Fig. 5, we can see that the value of $(\sigma_{yy})_{y=0.08mm}$ (110 MPa) in the grooved protruded specimens was lower than σ^* (126 MPa) for the near-interface TBC cracking in the ungrooved specimen. The value of σ_{yy}^m (162 MPa) in the ungrooved protruded specimen, which appeared in a TBC region slightly closer to the interface compared to the cracking site in the grooved specimens, nearly agreed with σ^* for the away-from-interface TBC cracking in the grooved specimen. These results explain why the different TBC cracking behavior can be ob-served in the protruded specimen without and with the grooved substrate.

The TBC cracking behavior near and away from the TBC/TGO interface is related to residual stresses distributed through the TBC thickness. It has been shown [12,13] that in-plane biaxial compressive residual stresses, which are counterbalanced by tensile components in the BC and substrate, are built-up during the thermal cycling due to the thermal expansion coefficient mismatch between the TBC and BC/substrate. Under the plane strain condition below the TBC surface, an out-of-plane compressive residual stress would be distributed through the TBC thickness, showing the peak near the midst TBC [10]. It is possible that the compressive residual stress, which is intensified near the root radius, offsets more σ_{yy} away from the interface, thereby increasing the value of σ^*. In order to clarify the effect of the compressive residual stress distributed through the TBC thickness, the position of a root radius, which controls the location of σ_{yy}^m and the site of crack initiation, was changed in the ungrooved and grooved protruded specimens. Such protruded tests demonstrated strong dependence of σ^* on the cracking site, defined by the distance from the TBC/BC interface (y_{ci}), in Fig. 6. Higher values of σ^* were observed near $y_{ci} = 0.1$ mm, compared to those near the TBC/TGO interface and TBC surface.

Machining the parts of substrate in the protruded specimen can relieve the residual stress of the TBC. The effect of residual stress on the in-plane TBC cracking can be also demonstrated
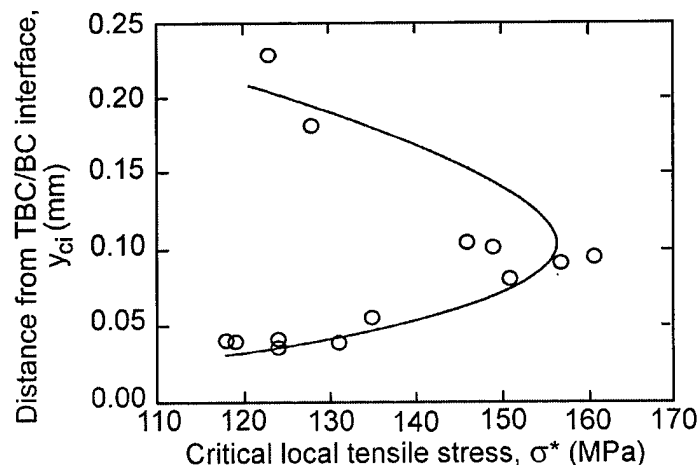

Figure 6. Variation of critical local tensile stresses for in-plane TBC crack initiation with distance from TBC/BC interface.

M9.15.5

by changing the substrate thickness [10]. The value of σ^* required for the near-interface TBC cracking decreased when the substrate thickness exceeded 1.2 mm. This means that tensile residual stress exists adjacent to the interface and is relaxed by reducing the substrate thickness less than 1.2 mm. Conversely, the TBC cracking away from the interface became more difficult in thicker substrate specimens. Increasing tensile and compressive residual stresses produces opposing effects on the TBC cracking.

CONCLUSIONS

The delamination behavior of thermal barrier coatings (TBC) was examined using a protruded four-point bending testing technique together with a finite element stress analysis. In four-point bending tests on protruded TBC specimens without and with grooved substrates, in-plane TBC cracks formed near and away from the interface of TBC/thermally grown oxides (TGO), respectively. It is evident from the cracking morphology that the near- and away-from-interface TBC cracking in the protruded TBC specimen were controlled by the out-of-plane tensile stress but not by the principal stress. The onset of TBC cracks near the TBC/TGO interface occurred at a lower critical local tensile stress than that away from the interface. The residual stress distribu-tion is taken into account to discuss the TBC delamination behavior near and away from the interface.

ACKNOWLEDGEMENTS

REFERENCES

1. J. T. DeMasi, K. D. Sheffler, and M. Ortiz, NASA Contract Report-182230 (1989).
2. S. M. Meier, D. M. Nissley, and K. D. Sheffler, NASA Contract Report-189111 (1991).
3. E. H., Jordan, M., Gell, D. M. Pease, L. Shaw, D. R. Clarke, V. Gupta, B. Barber and K. Vaidyanathan, *ASME Turbo Expo'97*, American Society of Mechanical Engineers, New York, NY (1997) GT-97-363.
4. P. G. Charalambides, J. Lund, A. G. Evans and R. M. McMeeking, J Appl. Mech., **56**, 77 (1989).
5. ASTM Standard C633-79 C, American Society of Testing Materials, Philadelphia, PA (1979).
6. C. J. Johnson, J. A. Ruud, R. Bruce, and D. Wortman, Surf. Coat. Technl., **108-109**, 80 (1998).
7. Z. Zhang, T. E. Bloomer, J. Kameda and S. Sakurai, *ASME Turbo'99*, American Society of Mechanical Engineers, NY (1999) GT-99-380.
8. Z. Zhang, T. E. Bloomer and J. Kameda, Contract Progress Report, Ames Laboratory, 1998.
9. Z. Zhang, T. E. Bloomer, J. Kameda and S. Sakurai, *Interfacial Engineering for Optimized Properties II*, edited by C. B. Carter, E. L. Hall, S. Nutt and C. L. Briant, Materials Research Society, Pittsburgh, PA (2000) p. 279.
10. Z. Zhang, J. Kameda, A. H. Swanson and S. Sakurai, to be published.
11. Z. Zhang, J. Kameda, A. H. Swanson and S. Sakurai, *Proc. Int. Con. Processing, Manufacturing of Advanced Materials: Thermec '2000*, TMS, Warendale, OH, in press.
12. P. Scardi, M. Leoni, L. Bertini, and L. Bertamini, Surf. Coat. Tech., **94-95**, 82 (1997).
13. A.M. Freborg, B. L. Ferguson, W. J. Brindley and G. J. Petrus, Mat. Sci. and Eng., **A245**, 182 (1998).

R&D Status and Needs for Improved EB-PVD Thermal Barrier Coating Performance

C. Leyens, U. Schulz, M. Bartsch and M. Peters
DLR-German Aerospace Center
Institute of Materials Research
51170 Cologne, Germany

ABSTRACT

The key issues for thermal barrier coating development are high temperature capability and durability under thermal cyclic conditions as experienced in the hot section of gas turbines. Due to the complexity of the system and the interaction of the constituents, performance improvements require a systems approach. However, there are issues closely related to the ceramic top coating and the bond coat, respectively. Reduced thermal conductivity, sintering, and stresses within the ceramic coating are addressed in the paper as well as factors affecting failure of the TBC by spallation. The latter is primarily governed by the formation and growth of the thermally grown oxide scale and therefore related to the bond coat. A strategy for lifetime assessment of TBCs is discussed.

INTRODUCTION

Since their first introduction into aerospace components in the late 1950s/early 1960s, thermal barrier coatings (TBCs) have matured from coatings for low-load applications on non-rotating parts, such as combustor liners, to systems for demanding applications on vanes and even leading edges of blades. Traditionally, TBCs were applied by flame spraying and subsequently by plasma spraying, whereas electron beam physical vapor deposition (EB-PVD) to deposit the ceramic coating has been used only since the 1980s. Today, typical TBC systems for turbine blades consist of a thermally insulating ceramic top coating (usually 100 to 300 μm partially yttria stabilized zirconia, PYSZ) deposited onto a superalloy substrate which is protected against environmental degradation by a metallic bond coat (either aluminide, Pt-modified aluminide or MCrAlY-type) (figure 1). Although the "bond coat" is by definition supposed to provide adhesion of the PYSZ top coating to the substrate, the real bonding layer between the ceramic

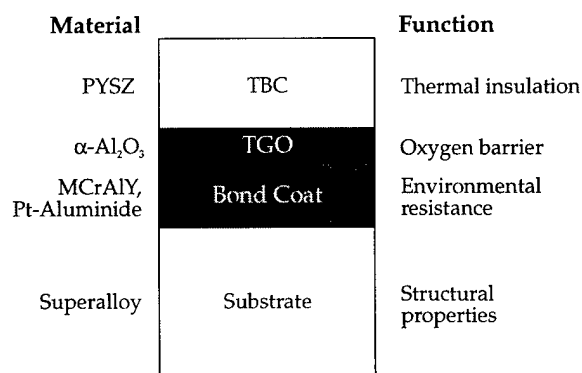| Material		Function
PYSZ	TBC	Thermal insulation
α-Al$_2$O$_3$	TGO	Oxygen barrier
MCrAlY, Pt-Aluminide	Bond Coat	Environmental resistance
Superalloy	Substrate	Structural properties

Figure 1. Schematic of a TBC system for hot section components in gas turbines.

M10.1.1

and the metallic coating is the thermally grown oxide (TGO), typically and preferably alumina that forms during processing and due to bond coat oxidation in service. The four constituents of a TBC system - substrate, bond coat, TGO, and PYSZ - are all dynamic in nature and interaction of the constituents during service affects system performance and durability.

From an engineering perspective, there are essentially two major design goals for TBCs, namely durability and performance improvement. Service conditions, materials properties and processing conditions greatly influence TBC durability and performance and also interact with each other, see figure 2, indicating a complex scenario that certainly requires a systems approach. Obviously, the ideal TBC system would combine improved component performance *and* coating durability, and the proper balance must be determined by technical and economical requirements. With regard to maximum performance, "designed-in TBC" solutions which are capable of utilizing the full insulating potential of the ceramic top coating (calculated to $\Delta T \approx 150K$, today) and which are deposited onto substrates used at their high temperature limits are certainly the ultimate engineering challenge. In this scenario, loss of the TBC would lead to rapid degradation of the component since failure of one part of the system would automatically result in overloading of another constituent. It is therefore clear that improved coating durability must be the major development goal with emphasis to spalling resistance of the top coating.

The present paper aims at a comprehensive discussion of the research and development status and needs for future generation EB-PVD TBCs and is primarily focused on ceramic top coat and bond coat issues. Processing-related performance and durability aspects will be highlighted as well as a strategy for lifetime assessment of TBC systems.
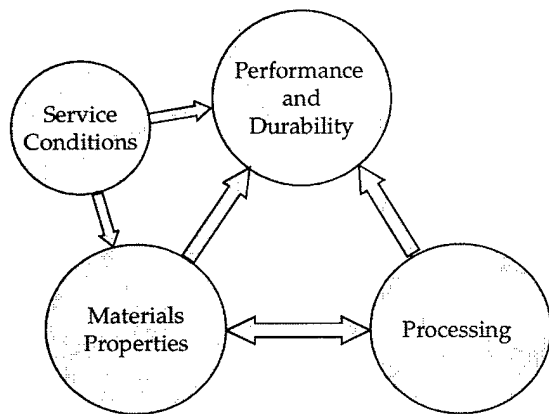
Figure 2. Factors affecting performance and durability of TBC systems.

ADVANCED CERAMIC COATINGS

The key features required for a material to become a thermal barrier coating are a reasonably low thermal conductivity and sufficient high temperature capability. There are numerous approaches to significantly improve these properties, both by materials development and sophisticated processing [1-5]. Alternative ceramics (other than state-of-the-art PYSZ) have increasingly gained interest, aiming at low conductivity and/or improved high temperature capability. As another example, intelligent processing has been used to tailor the inter- and

intracolumnar coating architecture towards low conductivity. Some of the most important issues will be discussed in the following.

Reduced thermal conductivity

In the early days of thermal barrier application, the major research and development focus was on feasibility and reliability issues [6], since coatings tended to spall and thus lost their protective properties. Today, thermal barrier coatings are well-engineered systems that can survive several ten thousand hours in service. Therefore, research has quite recently been directed to the thermal conductivity challenge more intensely [6-12]. Moreover, quite a number of patents have been filed and issued within the past two or three years, e.g. [2, 3, 5, 13-16], indicating considerable commercial interest and prospect in this area. Although there are considerable efforts to reduce thermal conductivity of plasma sprayed coating the following discussion will focus on EB-PVD TBCs only.

There are basically two routes to obtain low conductivity thermal barrier coatings. The first route is via alternative ceramics (either alternative stabilizer or matrix or both) with low inherent conductivities. With CeO_2-based ceramics [17], pyrochlore oxides such as lanthanum zirconate [18], yttrium aluminum garnet-based ceramics [19] or zirconia-containing first metallic oxides such as yttria, ytterbia, ceria, india, scandia or magnesia to stabilize the zirconia, second and third metallic oxides such as ceria, erbia, neodymia, gadolinia, dysprosia, europia, etc. to reduce the photon and phonon thermal conductivity of the coating [13, 15], a substantial reduction of thermal conductivity of the order of 50% relative to state-of-the-art TBCs is expected. However, most of these systems have not yet matured to commercial application, mainly due to lack of information about other important properties such as durability, producibility, etc.

In general, conductivity of coatings is usually lower than that of the bulk material due to incorporation of defects such as cracks and pores allowing phonon scattering and thus additional consumption of energy. Typical conductivities for EB-PVD YPSZ are of the order of 1.5-1.8 W/(m K) [6, 7, 20] which is roughly twice as high as that of plasma sprayed coatings, where initial values between 0.8-1.2 W/(m K) have been reported. This can be directly explained by the different coating microstructures. Whereas plasma sprayed TBCs exhibit a crack network mainly parallel to the coating surface as well as spheroidal porosity, EB-PVD coatings rely mainly on *intra*-columnar porosity while *inter*-columnar porosity is much less effective in lowering thermal conductivity. Important parameters regarding intracolumnar porosity to reduce thermal conductivity are size, distribution, concentration and morphology.

The second route to lower the thermal conductivity of EB-PVD TBCs is therefore by tailoring the microstructure to maximize energy consumption by phonon scattering. It is well known that the microstructure of EB-PVD TBCs strongly depends on processing parameters such as deposition temperature and rotational speed, vapor incidence angle etc. (see, e.g., [21-23]). Hence, microstructure tailoring is feasible, within limits, which might again be set by durability, processing cost issues, etc. In addition to the aforementioned microstructure modifications, multilayered coatings have been developed, using different approaches. One approach is to apply a multilayer TBC with alternating layers of, e.g., zirconia and alumina [5], yttria stabilized zirconia and hafnia [1], or yttria and ceria [2]. With these systems, there are at least two factors contributing to a reduced thermal conductivity: firstly, thin films have been reported to exhibit lower thermal conductivities than the respective bulk materials [6], and secondly, additional boundaries are incorporated perpendicularly aligned to the heat flux. A slightly different approach is to deposit multilayered TBCs with different porosity levels in single layers [16].

Moreover, TBC columns arranged at an acute angle to the surface of the substrate combined with porosity variations in the multilayer coating [16] as well as microstructures replicating a herringbone or zigzag pattern [24] have demonstrated reduced thermal conductivities.

Typically, all these microstructure modifications can be obtained by sophisticated processing. However, the major challenge is to maintain the initial advantages of reduced conductivity over a long service life at high temperatures. For example, nano-scaled multilayers consisting of zirconia and alumina were reported to lose their beneficial effect relatively shortly during high-temperature exposure [20]. A method to partly circumvent this degradation is to apply a multilayered microstructure near the bond coat/ceramic top coat interface where temperatures must be comparably low (of the order of 1000°C) due to bond coat and substrate temperature limitations. One shortcoming of the latter approach is certainly, that other beneficial effects of multilayered TBCs, such as improved erosion resistance [5], might not be fully utilized. Another typical problem associated with maintaining low thermal conductivity at high temperatures is sintering of the ceramic; this will be addressed below in more detail.

Increased temperature capability

Thermal stability of the ceramic top coating becomes a concern for state-of-the-art TBC systems when surface temperatures of the ceramic exceed about 1200°C. The t' phase in YPSZ coatings decomposes into t_1+t'+c with some traces of m after a few hundred hours at 1200°C and even within several ten hours at 1300°C [25]. For technical applications, formation of monoclinic phase is of serious concern, since phase transformation from t' to m is associated with a volume change of the order of 4 to 5 % which places a significant threat on the integrity of the ceramic coatings. Therefore, higher surface temperatures anticipated in future gas turbines require ceramic coatings with increased phase stability although recent results have shown that considerable amounts of monoclinic phase in the as-processed coating can be tolerated for EB-PVD coatings [26].

Apart from destabilization issues of zirconia-based TBCs, enhanced sintering of the columnar microstructure is a serious concern at high temperatures. At surface temperatures of the ceramic top coating relevant for aeroengine applications, YPSZ sinters quite significantly. Intercolumnar sintering increases the Young's modulus of the ceramic (typically of the order of 50-100 GPa in the as-coated condition [21]; a brief literature survey is provided in [27]) and thus stresses in the ceramic top coating increase during service. The additional elastic energy stored in the ceramic provides further driving force for crack initiation and propagation and promotes spalling of the coating [28]. Moreover, sintering effects also reduce intracolumnar porosity and thus increase thermal conductivity. If reduction of thermal conductivity is anticipated to primarily rely on microstructural optimization, excellent sintering resistance is required to maintain low conductivity during long-term application.

Therefore, new ceramic materials are increasingly under consideration. For example, ceria-stabilized coatings have been reported to have higher temperature capability than yttria-stabilized zirconia. Moreover, scandia/yttria-stabilized zirconia, where scandia substitutes for 90% of the yttria [29], is considered as a promising candidate material capable of exceeding the "magic" temperature limit of presently 1200°C. Replacing zirconia by hafnia results in a reduced sintering tendency in the temperature regime between 1100 and 1400°C [30]. However, quite obviously, searching for a new ceramic material requires a systems approach, both in a narrow and a wide sense, taking into account thermo-physical properties (mainly thermal conductivity and thermal expansion), phase stability, sintering and erosion resistance as well as chemical inertness against

combustion atmosphere, chemical compatibility with the bond coat and/or the alumina etc. Moreover, the use of a new material might be limited by economic considerations such as the cost of raw material and additional processing cost. Due to great vapor pressure differences of the constituents of some candidate materials, sophisticated processing is necessary to control the chemistry of the coating during EB-PVD deposition. Multiple-source high rate coaters are considered a valuable tool to overcome this problem. Evaporation is then performed from chemically well-controlled sources containing low and high vapor pressure constituents, and the desired coating chemistry is achieved by mixing of the species in the vapor phase as well as during coating growth [27, 31]. For industrial production, this fabrication method brings about additional issues to overcome, one of them might be to obtain chemical uniformity over a large volume in the coater.

Reduced stresses in the ceramic top coating

As mentioned above, stresses in the ceramic coating are one contributor to coating failure by spallation (however, stresses in the TGO are held to be equally or even more important, as will be discussed below). A major cause of stresses in TBC systems is the mismatch of the coefficients of thermal expansion (CTE) of the single layers. Whereas the CTE of YPSZ is of the order of $10x10^{-6}$ K^{-1}, the superalloy substrates exhibit higher CTEs of $16x10^{-6}$ K^{-1}. These differences result in compressive stresses within the YPSZ layer upon cooling, the extent of which depends on the elastic modulus of the material; with increasing modulus, the residual stresses within the coating increase (stresses were reported in the 20-300MPa range) [21]. Modifiying the YPSZ microstructure towards low elastic moduli is one avenue to take, another is to tailor the bond coat-YPSZ interface to reduce stresses near this interface. Chemical or density grading of the ceramic coating have been proposed [32, 33] but the longevity of these systems at high temperatures is still insufficient. Phase transformations in the ceramic are another source of stresses and must therefore be avoided. Candidates for alternative stabilizers that suppress phase transformation and/or alternative ceramics have been discussed above.

ADVANCED BOND COATINGS

The primary design goal of advanced TBCs is enhanced durability, particularly resistance against loss of the ceramic top coating by spallation. Coating spallation might be induced by various factors, including particle erosion, cracking within the ceramic top coating (usually intercolumnar crack propagation) and cracking at or near the bond coat-YPSZ interface. Whereas the first two types of failure typically lead to successive or partial degradation of the TBC, interfacial cracking is a prime concern because it eventually leads to spallation of major parts or of the entire TBC. Some important factors promoting cracking associated with deleterious changes within the ceramic have already been discussed above (phase transformation and sintering). The following paragraphs focus on bond coat-related issues that strongly affect TBC lifetime. It is meanwhile well accepted that formation and continued growth of the TGO associated with bond coat oxidation during processing and during service is a critical factor controlling the durability of a TBC system. Although there is not a generic, well-defined failure location for various TBC systems being in use today, EB-PVD coatings are usually reported to fail at or near the bond coat-YPSZ interface (see, for example [28, 34, 35]), indicating that the TGO is the weakest link in the system.

Though it is considerably easy to name the requirements for an optimal-performing TGO (which are essentially a slow growth rate and sufficient adhesion during thermal cyclic loading), a significant amount of research has been placed on the understanding of failure mechanisms and the factors contributing to spallation of the oxide scale, either with or without a ceramic top coating. The following paragraphs will highlight some of the important findings. In some cases improved understanding of oxide scale adhesion and/or failure has resulted in improved TBC performance.

TGO and TBC failure modes and mechanisms

Among numerous materials and processing variables, the localized stress and the interface strength in the vicinity of the TGO appear to be two of the most important ones in promoting failure [36, 37]. Jordan et al. [37] proposed a model providing a simplistic description of the debonding process of the TGO. More sophisticated and accurate approaches that involve fracture mechanics have been proposed by Evans et al. [34, 38], using interface toughness and strain energy release rate as quantitative measures. The simplistic model for TGO debonding involves the bond strength of the TBC (or TGO) and the bond stress. Although coatings are usually optimized for maximum initial bond strength and minimum out-of-plane stresses, in general, the bond strength degrades and the bond stresses increase with time and cycles in the engine [36].

Bond strength measurements of EB-PVD TBCs deposited onto Pt-Al bond-coated single crystal superalloy René N5 using a modified ASTM direct pull test revealed a strong decline in bond strength within a fairly small number of cycles (figure 3a) [36]. Very similar behavior was observed for EB-PVD TBCs on IN 617 overlaid with an EB-PVD Ni-Co-Cr-Al-Y bond coating (figure 3b). Here, the maximum strain to failure was determined in four-point-bending tests on single-side coated beams after isothermal exposure at 1000 and 1050°C in air up to 1013h. Again, strain to failure (which is supposed to be a qualitative measure of the bond strength of the
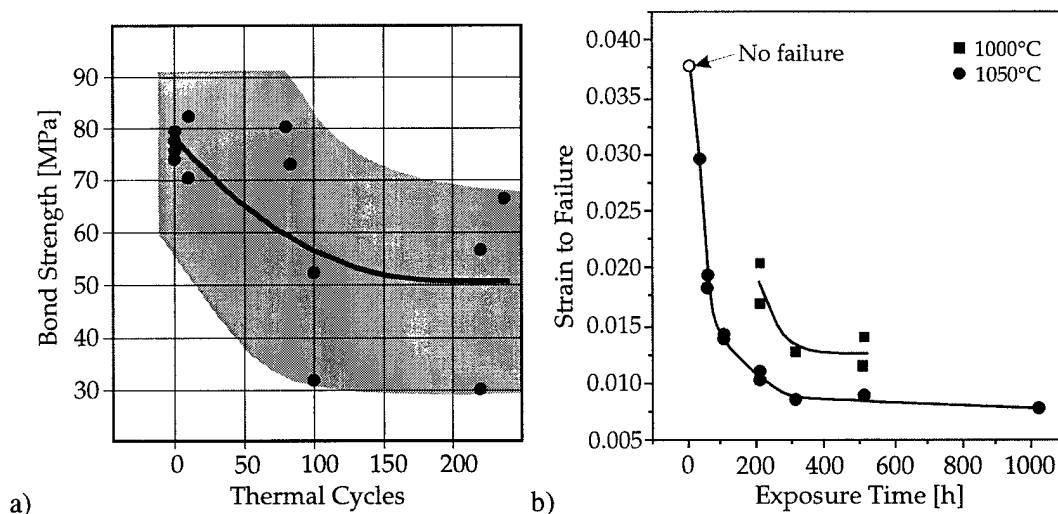

Figure 3. (a) *Bond strength of an EB-PVD TBC on Pt-Al coated René N5 with thermal cycling at 1121°C (2050°F)* [36]. *Data was determined using a modified ASTM pull test.* (b) *Strain to failure vs. Exposure time at 1000 and 1050°C for EB-PVD TBCs on Ni-Co-Cr-Al-Y coated IN 617. Notably, strain to failure drops strongly after short annealing times.*

coating) declined rapidly during short exposure times but then almost settled down to a constant value up to 1013h. Although only a few bars were exposed at 1000°C, the trend of strain to failure curve is very similar to that for bars exposed at 1050°C. As expected, at the lower temperature, degradation of the coating is shifted towards longer exposure times and somewhat higher strains. These results indicate that degradation processes already occur after short times of exposure.

The reason for rapid degradation of adhesion is still not fully understood. Processing-related phenomena are considered to be potential contributors. For example, TEM investigation of the bond coat-TGO-TBC interface region revealed that a mixture of zirconia and alumina can be formed right after or during EB-PVD processing (figure 4) [39]. The distribution of zirconia particles within the alumina matrix can either be uniform (figure 4a) or segmented (figure 4b) with areas of virtually pure alumina just next to mixed zones containing alumina and zirconia. Formation of this mixed TGO layer and its dependence on processing conditions is currently carefully studied and will be the subject of a companion paper [40]. Moreover, the contribution of the mixed TGO layer to rapid degradation of adhesion of the TBC is still under investigation. For weak bond coat-TGO interfaces, cracking can occur within or near the mixed oxide layer which finally leads to spallation of the ceramic top coating [35]. However, failure at this interface was observed after extended exposure times only, when extensive pore formation occurred within the mixed TGO layer; therefore, more work is needed to assess the effect of a mixed alumina-zirconia TGO on the adhesion and ultimately the lifetime of EB-PVD TBCs.
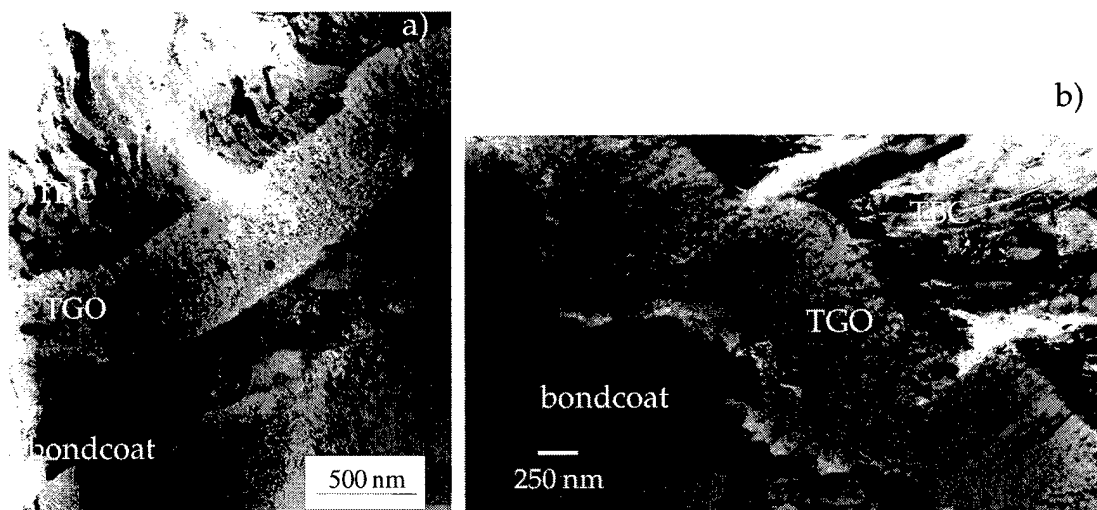
Figure 4. TEM cross section of as-deposited EB-PVD thermal barrier coatings with (a) uniform distribution of zirconia particles in an alumina matrix and (b) segmented pure alumina and alumina-zirconia TGO.

Bond coats with improved durability

As discussed in the previous sections, bond coat performance is crucial for TBC durability, and both chemical and mechanical aspects substantially affect adhesion of the oxide scale on long-term exposure. Undoubtedly, the overview was by far not complete and in the following

only two avenues taken to improve bond coat performance are briefly described. There is much more room for improvement than will be mentioned here, especially if processing-related issues are considered, which is beyond the scope of this paper.

Since the thermal expansion mismatch between the substrate/bond coat and the TGO is a major contributor to TBC spallation, adjusting the coefficient of thermal expansion of the bond coat to that of the substrate and the TGO might be a fruitful concept for improved spallation resistance under cyclic conditions [28, 41], especially when the wall thicknesses of components such as modern airfoils are thin and thermal expansion of the bond coat makes a major contribution to the overall expansion of the component. Moreover, measures to lower the coefficient of thermal expansion and strengthen the bond coat at the same time, for example by incorporation of dispersed particles such as Al_2O_3, $Cr_{23}C_6$ and precious metals, have demonstrated to improve cyclic oxidation resistance substantially [42].

Improving the oxidation resistance of the bond coats (i.e. providing bond coats with a slow growth rate for very long exposure times and with excellent adhesion) is certainly the major goal for bond coat development. It appears that recently increasing attention was directed towards development of advanced aluminide coatings. Properly doped nickel aluminides were shown to have a much better spallation resistance than M-Cr-Al-Y-type alloys [43, 44], especially at higher temperatures. Noteworthy, it appears that Pt currently added to improve oxidation and spallation resistance of nickel aluminide coatings might be unnecessary, if proper doping with Hf or other reactive elements can be achieved [44]. Oxidation tests on cast nickel aluminides demonstrated that Hf-doped NiAl outperformed the Pt-containing variants in terms of growth rate and spallation resistance [44, 45]. Co-doping might give even more room for improvement, but the potentials have not yet been explored to a great extent.

LIFETIME ASSESSMENT STRATEGIES

The TBC system as well as the loading conditions in service are quite complex. Thus, the failure mechanisms and microstructure-level mechanics are not clearly understood. For the final stage before spallation, elaborated mechanism-based approaches to assess the durability of TBCs have been developed [46]. Requirements for further progress in mechanism-based approaches are outlined in [34]. Particularly the lack of methods to probe the degradation of resistance against damage evolution before large scale separations occur hinders the development of a fully linked mechanism-based model for the lifetime assessment of TBCs.

On the other hand so-called 'engineering models' based on Manson-Coffin type damage accumulation rules were developed [47, 48]. In these concepts, damage evolution is described by empirical damage parameters related to certain damage mechanisms. The evolution of the damage parameters as a function of kinetics or number of load alternations was determined separately in simplified experiments. Subsequently, the contribution of every damage mechanism to the consumption of TBC life under more complex testing conditions was accumulated. For example, in [47], the thickness of the TGO as a time-at-high-temperature dependent damage parameter is related to the degree of damage due to oxidation of the bond coat. TGO growth kinetics were determined in oxidation experiments; in burner rig tests the decrease of number of thermal cycles to failure due to TGO growth was measured. The results of the burner rig tests supplied fit parameters for the cumulative damage rule. However, service conditions are more complex and consequently the number of parameters which have to be taken into account for estimating the TBC lifetime is reasonably high. Additional fitting parameters are needed to include interaction effects of the different mechanisms. The required high number of parameters

to describe the damage situation makes this concept impractical for lifetime assessment under service conditions. Furthermore, different TBC systems are in use, thus for mechanism related lifetime assessment models the dominating mechanisms and appropriate damage parameters for each system have to be identified.

In order to get a practical lifetime assessment for TBC systems, also methods are required which do not need the explicit description of damage evolution due to single mechanisms. Instead of accumulating the contributions of separate damage mechanisms determined in simplified tests, the lifetime assessment described in [49] is based on the accumulated damage under realistic testing conditions. The idea behind is to ensure that the damage mechanisms including interaction effects in testing are identical to that in service. However, it is impractical to simulate a service cycle in real time, since turbine blades in modern gas turbines in aircraft engines are designed for about long service life of the order of thousands of hours. The time for one test cycle can be decreased drastically if number-of-cycle dependent fatigue damages are determined separately from damages caused by kinetic mechanisms because fatigue damages are induced by changes of the load and not by the dwell time on a certain load level. Damages induced by time-at-high-temperature dependent kinetic mechanisms will be considered by testing heat-treated specimens. The test facility for fatigue testing simulates the loading conditions of turbine blades in an aircraft engine during a whole flight, including thermal shock due to start and shut down of the engine and the thermal gradient from the surface to the internally cooled inner wall of the blade. Hollow cylindrical specimens are used. The so-called thermal gradient mechanical fatigue (TGMF) test facility and the specimens are described in detail in [49]. The time for one test cycle representing the load alternations of one flight is about 1 to 3 minutes.

First testing results revealed that the as-coated properties of EB-PVD TBC systems are sufficient to survive the required number of load alternations during service life (figure 5). All TBC-coated samples exceeded the number of cycles of the bond-coat-only samples although the reference temperature at the bond coat outer surface was kept constant to establish comparable loading conditions. Obviously, the TBC surface temperature was higher than that of the bond coat only sample. The conclusion from these results is that premature failure of TBCs observed in service is due to time-at-high-temperature dependent kinetic mechanisms. Fatigue damages due
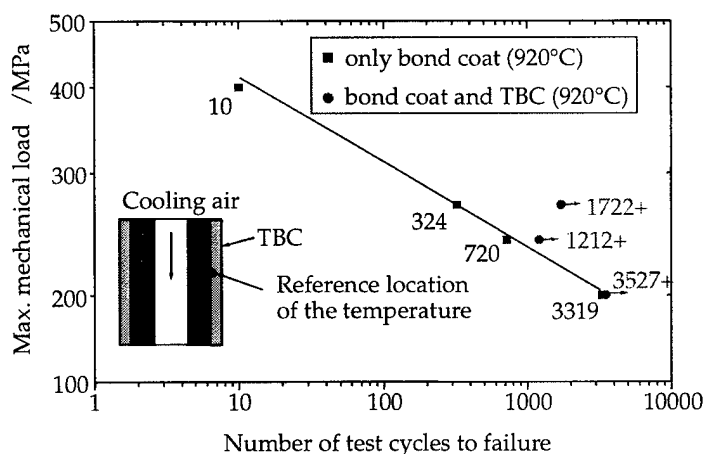
Figure 5. Maximum load vs. number of test cycles to failure for bond coated only and bond coat plus TBC samples. Results indicate that TBCs survive number of cycles required from a fatigue damage perspective.

M10.1.9

to cycling are supposed to reduce TBC lifetime simultaneously to damages by time-at-high-temperature dependent kinetic processes. To determine the interaction effects between fatigue and kinetic damage mechanisms the lifetime of pre-aged specimens in TGMF-tests with short cycle-time will be compared with the lifetime of as coated specimens in TGMF-testing with extended dwell times.

This engineering approach to lifetime assessment of TBCs has several strong points. It is applicable to different TBC material systems since no damage parameters related to individual material dependent mechanisms have to be determined. Nevertheless it must be ensured that the failure causing damage mechanisms in testing are the same like in service. Thus, the failure mechanisms in service and in testing have to be identified e.g. by means of microstructural investigations. The testing parameters must be adapted to the failure relevant service condition of the component. However, these testing parameters, e.g. temperature, mechanical load, heat flux, number of engine starts, and dwell times, are the design parameters for the whole component. Thus, it is convenient to use the lifetime assessment based on TGMF testing to integrate the TBC into the component design.

SUMMARY

Significant performance improvements of today's well-engineered thermal barrier coating systems require a systems approach including all constituents of the complex multilayered material. For the ceramic coating an increased high temperature capability that requires ultimate phase stability and low sintering activity as well as low thermal conductivity are the key design goals. The main issue with the use of TBCs in demanding gas turbine applications is durability, i.e. essentially resistance against spallation of the insulating top coating. Spallation of the TBC in EB-PVD systems is closely related to oxidation phenomena of the bond coat. Therefore, slow oxidation rates and ultimate oxide scale adhesion are the key design goals for bond coat development. Research and development efforts worldwide are underway to gain detailed and quantitative information about TBC durability, finally aiming at developing reliable life-prediction models that will allow to use TBCs at their limits to gain maximum benefit. A strategy for lifetime assessment via thermal gradient fatigue testing is discussed.

ACKNOWLEGMENTS

REFERENCES

1. W.A. Kaysser, T. Krell, M. Bartsch, C. Leyens, U. Schulz and M. Peters, *Surface Engineering EUROMAT '99*, ed. H. Dimigen, (Wiley-VCH, 2000), pp.3-12.
2. M.J. Maloney, U. S. Patent 6,007,880, 1999.
3. M.J. Maloney, U. S. Patent 6,057,047, 2000.
4. U. Schulz, K. Fritscher and C. Leyens, *Surface and Coatings Technology*, **133-134**, 40-48 (2000).
5. D. Wortman, U.S. Patent 5,942,334, 1999.
6. S. Alperine, M. Derrien, Y. Jaslier and P. Mevrel, AGARD R-823, 1-1/1-10 (1997).
7. R.B. Dinwiddie, S.C. Beecher and W.D. Porter, The effect of thermal aging on the thermal conductivity of plasma sprayed and EB-PVD thermal barrier coatings

International Gas Turbine and Aeroengine Congress & Exhibition (The American Society of Mechanical Engineers, 1996).

8. J.-M. Dorvaux, O. Lavigne, R. Mevrel, M. Poulain, Y. Renollet and C. Rio, AGARD R-823, 13-1/13-10 (1997).

9. P.G. Klemens and G. M., *Materials Science and Engineering*, **A245**, 143-149 (1998).

10. J.R. Nicholls, K.J. Lawson, D.S. Rickerby and P. Morrell, AGARD R-823 Report, 6-1/6-9 (1997).

11. K.S. Ravichandran, K. An, R.E. Dutton and S.L. Semiatin, AGARD R-823 Report, 14-1/14-12 (1997).

12. R.E. Taylor, *Materials Science and Engineering*, **A245**, 160-167 (1998).

13. D.S. Rickerby, P. Morrel and Y.A. Tamarin, Europe Patent EP 0 825 271 A1, 1997, filed.

14. S.A. Alperine, S. Gerzdev, Y.-P. Jaslier and Y. Tamarin, Europe Patent EP 0 990 716 A1, 1999, filed.

15. D.S. Rickerby, P. Morrell and Y.A. Tamarin, U. S. Patent 6,025,078, 2000.

16. D.S. Rickerby, Europe Patent EP 0 902 104 A2, 1998, filed.

17. M. Maloney, H. Achter and B. Barkalow. Development of low conductivity thermal barrier coatings, *TBC Workshop*, (1997).

18. M.J. Maloney, Europe Patent EP 0 992 603 A1, 1999, filed.

19. N.P. Padture, M. Gell and P.G. Klemens, U. S. Patent 6,015,630, 2000.

20. T. Krell, Thermische und thermophysikalische Eigenschaften von elektronenstrahlgedampften chemisch gradierten Al2O3/PYSZ-Wärmedämmschichten, Ph.D. thesis, *VDI-Fortschritt-Berichte*, (VDI-Verlag, 2001, in press).

21. C.A. Johnson, J.A. Ruud, R. Bruce and D. Wortman, *Surface and Coatings Technology*, **108-109**, 80-85 (1998).

22. S.G. Terry, J.R. Litty and C.G. Levi, Evolution of porosity and texture in thermal barrier coatings grown by EB-PVD, *Elevated Temperature Coatings: Science and Technology III*, ed. J.M. Hampikian and N.B. Dahotre, (TMS, 1999), pp. 13-25.

23. U. Schulz, *Wachstum, Mikrostruktur und Lebensdauer von elektronenstrahlaufgedampften Wärmedämmschicht-Systemen für Turbinenschaufeln*, in *Bergakademie Freiberg*, Ph.D. thesis, (Verlag Shaker, 1995).

24. G.H. Marijnissen, A.H.F. van Lieshout, G.J. Ticheler, H.J.M. Bons and M.L. Ridder, U.S. Patent 5,876,860, 1999.

25. U. Schulz, *Journal of the American Ceramic Society*, **83**, 904-910 (2000).

26. R.W. Bruce, D.J. Wortman, R. Viguie and D.W. Skelly, U. S. Patent 5,081,088, 1999.

27. U. Schulz, K. Fritscher, C. Leyens and M. Peters, Influence of processing on microstructure and performance of EB-PVD thermal barrier coating, *ASME Turbo Expo 2000*, (ASME, 2000), paper no. 2000-GT-0579.

28. M.J. Stiger, N.M. Yanar, M.G. Topping, F.S. Pettit and G.H. Meier, *Zeitschrift für Metallkunde*, **90**, 1069-1078 (1999).

29. R.L. Jones, U. S. Patent 6,044,830, 2000.

30. D. Zhu and R.A. Miller, *Surface and Coatings Technology*, **108-109**, 114-120 (1998).

31. U. Schulz, K. Fritscher, C. Leyens and M. Peters, *JOM-e*, **49**, (1997).

32. T. Krell, U. Schulz, M. Peters and W.A. Kaysser, *Materials Science Forum*, **308-311**, 396-401 (1999).

33. U. Leushake, K. T., U. Schulz, M. Peters, W.A. Kaysser and B.H. Rabin, *Surface and Coatings Technology*, **94-95**, 131-136 (1997).

34. P.K. Wright and A.G. Evans, *Current Opinion in Solid State and Materials Science*, **4**, 255-265 (1999).

35. C. Leyens, U. Schulz, B.A. Pint and I.G. Wright, *Surface and Coatings Technology*, **120-121**, 68-76 (1999).

36. M. Gell, E. Jordan, K. Vaidnanathan, K. McCarron, B. Barber, Y.-H. Sohn and V.K. Tolpygo, *Surface and Coatings Technology*, **120-121**, 53-60 (1999).

37. E.H. Jordan, M. Gell, D.M. Pease, L. Shaw, D.R. Clarke, V. Gupta, B. Barber and K. Vaidyanathan. *Bond strength and stress measurements in thermal barrier coatings*. 1997: American Society of Mechanical Engineers

38. A.G. Evans, M.Y. He and J.W. Hutchinson, *Acta Materialia*, **45**, 3543-3554 (1997).

39. Y.Q. Yang, C. Leyens, U. Schulz, H.J. Dudek and W.A. Kaysser. TEM Studies on thermally grown oxides of EB-PVD thermal barrier coatings, *Proc. Materials Week 2000*, (Wiley -VCH, 2000, in press).

40. C. Leyens, U. Schulz, W. Braue and Y.Q. Yang, (2001, in preparation).

41. C. Leyens, K. Fritscher, M. Peters and W.A. Kaysser, *Oxidation of Metals*, **34**, 329-352 (1995).

42. T.A. Taylor and D.F. Bettridge, *Surface and Coatings Technology*, **87088**, 9-14 (1996).

43. B.A. Pint and I.G. Wright, Cyclic Oxidation Behavior of Cast NiCrAl Alloys, *High Temperature Corrosion and Materials Chemistry*, ed. P.Y. Hou, *et al.*, (Electrochemical Society, 1998), pp. 263-274.

44. C. Leyens, B.A. Pint and I.G. Wright, *Surface and Coatings Technology*, **133-134**, 15-22 (2000).

45. B.A. Pint, J.A. Haynes, K.L. More, I.G. Wright and C. Leyens, Compositional effects on aluminide oxidation performance: objectives for improved bond coats, *Superalloys 2000*, (TMS, 2001, in press).

46. M.Y. He, A.G. Evans and J.W. Hutchinson, *Acta Materialia*, **45**, 3481-3489 (1997).

47. S.M. Meier, D.M. Nissley, K.D. Sheffler and T.A. Cruse, *ASME Journal of Engineering for Gas Turbines and Power*, **114**, 258-263 (1992).

48. R.A. Miller, *Journal of the American Ceramic Society*, **67**, 517-521 (1984).

49. M. Bartsch, G. Marci, K. Mull and C. Sick, Lifetime prediction of ceramic thermal barrier coatings based on lifetime analyses of close to reality test, *Proc. 7th Int. Symposium on Ceramic Materials and Components for Engines*, 2000, in press.